Matrix and Tensor-based ESPRIT Algorithm for Joint Angle and Delay Estimation in 2D Active Broadband Massive MIMO Systems
AND
Analysis of Direction of Arrival Estimation Algorithms for Basal Ice Sheet Tomography

By

Yi Zhu

Submitted to the Electrical Engineering and Computer Science Department and the
Graduate Faculty of the University of Kansas
in partial fulfillment of the requirements for the degree of
Master of Science

Dr. Lingjia Liu, Chairperson

Committee members

Dr. John Paden

Dr. Erik Perrins

Dr. Shannon Blunt

Date defended: August 6, 2014

The Dissertation Committee for Yi Zhu certifies
that this is the approved version of the following dissertation :

Matrix and Tensor-based ESPRIT Algorithm for Joint Angle and Delay Estimation in 2D Active Broadband Massive MIMO Systems
AND
Analysis of Direction of Arrival Estimation Algorithms for Basal Ice Sheet Tomography

Dr. Lingjia Liu, Chairperson

Dr. John Paden

Dr. Erik Perrins

Dr. Shannon Blunt

Date approved: August 6, 2014

Abstract

In this thesis, we apply and analyze three direction of arrival algorithms (DoA) to tackle two distinct problems: one belongs to wireless communication, the other to radar signal processing. Though the essence of these two problems is DoA estimation, their formulation, underlying assumptions, application scenario, etc. are totally different. Hence, we write them separately, with ESPRIT algorithm the focus of Part I and MUSIC and MLE detailed in Part II.

For wireless communication scenario, mobile data traffic is expected to have an exponential growth in the future. In order to meet the challenge as well as the form factor limitation on the base station, 2D massive MIMO has been proposed as one of the enabling technologies to significantly increase the spectral efficiency of a wireless system. In massive MIMO systems, a base station will rely on the uplink sounding signals from mobile stations to figure out the spatial information to perform MIMO beamforming. Accordingly, multi-dimensional parameter estimation of a ray-based multipath wireless channel becomes crucial for such systems to realize the predicted capacity gains. In the first Part, we study joint angle and delay estimation for 2D massive MIMO systems in mobile wireless communications. To be specific, we first introduce a low complexity time delay and 2D DoA estimation algorithm based on unitary transformation. Some closed-form results and capacity analysis are involved. Furthermore, the matrix and tensor-based 3D ESPRIT-like algorithms are applied to jointly estimate angles and delay. Significant improvements of the performance can be observed in our communication scheme. Finally, we found that azimuth estimation is more vulnerable compared to elevation estimation. Results suggest that the dimen-

sion of the antenna array at the base station plays an important role in determining the estimation performance. These insights will be useful for designing practical massive MIMO systems in future mobile wireless communications.

For the problem of radar remote sensing of ice sheet topography, one of the key requirements for deriving more realistic ice sheet models is to obtain a good set of basal measurements that enables accurate estimation of bed roughness and conditions. For this purpose, 3D tomography of the ice bed has been successfully implemented with the help of DoA algorithms such as MUSIC and MLE techniques. These methods have enabled fine resolution in the cross-track dimension using synthetic aperture radar (SAR) images obtained from single pass multichannel data. In Part II, we analyze and compare the results obtained from the spectral MUSIC algorithm and an alternating projection (AP) based MLE technique. While the MUSIC algorithm is more attractive computationally compared to MLE, the performance of the latter is known to be superior in most situations. The SAR focused datasets provide a good case study to explore the performance of these two techniques to the application of ice sheet bed elevation estimation. For the antenna array geometry and sample support used in our tomographic application, MUSIC performs better originally using a cross-over analysis where the estimated topography from crossing flightlines are compared for consistency. However, after several improvements applied to MLE, i.e., replacing ideal steering vector generation with measured steering vectors, automatic determination of the number of scatter sources, smoothing the 3D tomography in order to get a more accurate height estimation and introducing a quality metric for the estimated signals, etc., MLE outperforms MUSIC. It confirms that MLE is indeed the optimal estimator for our particular ice bed tomographic application. We observe that, the spatial bottom smoothing, aiming to remove the artifacts made by MLE algorithm, is the most essential step in the post-processing procedure. The 3D tomography we obtained lays a good foundation for further analysis and modeling of ice sheets.

Acknowledgements

I wish to extend my deepest gratitude to my advisor Dr. Lingjia Liu for his encouragement, guidance and patience during the course of this thesis. The experience I have gained during my association with both ITTC and CReSIS has been invaluable. I would also like to thank Dr. John Paden, Dr. Shannon Blunt and Dr. Erik Perrins for their time and kindness to serve on the committee, and helpful advise towards the fulfilment of the dissertation. Especially to Dr. John Paden, I am extremely grateful for the work opportunity he provided, the practical programming skills he taught and enormous help during my writing of second part of the thesis. My sincere gratitude to Dr. Victor Frost and Pam Shadoin for being patient and affording me an opportunity to complete this work. I also want to thank Dr. David Petr and Dr. Sam Shanmugan for their wonderful courses, which benefits me a lot for my future study. Finally, I would like to thank my parents, my girlfriend and all my friends in University of Kansas for their constant encouragement and immense support.

Contents

List of Figures

List of Tables

Part I

Matrix and Tensor-based ESPRIT Algorithm for Joint Angle and Delay Estimation in 2D Active Broadband Massive MIMO Systems

Chapter 1

Introduction

Rarely have technical innovations changed everyday life as rapidly and profoundly as mobile wireless communications. According to the International Telecommunication Union (ITU) [1], the number of mobile wireless subscriptions globally reached 6.8 billions in 2013, almost as many as the world population 7.1 billions. As a result, in February 2013, Cisco Systems predicted a staggering 66% compound annual growth rate (CAGR) for global mobile data traffic from 2012 to 2017 [2]. This is an 13-fold increase in wireless traffic over a five-year period.

A key societal question and a pressing engineering challenge is: "How can we support the predicted exponential growth in mobile data traffic?" To meet the increasing traffic demand, other than reallocating radio spectrum to wireless providers, spectral efficiency will need to be improved significantly. Multiple-input-multiple-out (MIMO) technology, together with Orthogonal frequency-division multiplexing (OFDM), offer efficient ways to increase the spectral efficiency of a mobile broadband communication system [3]. Recently, a new MIMO paradigm called "massive MIMO" has generated much interests in both academia [4, 5] and industry [6]. Using information theoretical analysis, it can be shown that even with random user scheduling and no inter-cell cooperation, unprecedented spectral efficiency in time-division-duplex (TDD) cellular systems can be achieved if a sufficiently large number of transmit antennas are employed at each base station.

Because of the sensitivity of MIMO algorithms with respect to the channel matrix properties,

channel modeling is particularly critical to assess the performance of underlying MIMO systems. The parametric channel model could be adopted by performing virtual direction-of-arrival (DoA) and direction-of-departure (DoD) estimation of resolvable paths. It provides a simple geometric interpretation of the scattering environment to characterize the two key MIMO channel metrics: ergodic capacity and diversity level [7]. Despite the advantage of reducing the number of estimation parameters, it is shown in [8] that channel estimation based on DoA and DoD provides the best performance in terms of the error bound.

Due to the form factor limitation, two-dimensional (2D) MIMO systems are introduced regarding elevation and azimuth domain, to fit a large number of antenna elements on the base station in reality. For a base station equipped with such planar arrays, it needs to know the corresponding multi-dimensional channel knowledge. There are many existing subspace-based methods such as MUSIC (MUltiple SIgnal Classification), ESPRIT and matrix pencil to estimate the one-dimensional (1D) DoA under parametric channel models. However, its counterpart in 2D, together with delay estimation is not yet well explored. The TST-MUSIC algorithm proposed in [9] have great performance in estimating the DoAs and delay of a wireless multi-ray channel, but the pairing of the 2-D angles and delay can't be automatically determined, which means two signals with close parameters are indistinguishable. In [10], the authors just show the M-dimensional estimation of spatial frequencies using tensor modeling without mentioning the individual physical parameters estimation, which are crucial for practical MIMO transceiver design.

The main reason why we choose ESPRIT algorithm over MUSIC is the existence of MIMO antenna array at the base station. ESPRIT has made signal-subspace based methods more attractive for implementation because the array manifold matrix need not be known and the search procedure is replaced by a simple eigenvalue problem. Especially when there are plenty of sensors compared with the number of sources to detect, ESPRIT is much more suitable than MUSIC and MLE with respect to the computational burden. Though for minimum squared error (MSE) perspective, MLE and MUSIC outperforms ESPRIT in most circumstances. Generally, we are satisfied with the results obtained from ESPRIT since it is also a super-resolution estimation technique.

Hence, in our paper, we define a natural tensor-based system model for the application of joint angle and delay estimation (JADE) and intense computer simulations are conducted. By jointly estimating the channel parameters, DoA estimation could give us accurate spatial information about the four-dimensional (4D) underlying physical channel which is crucial for transmit precoding. Simulation results indicate the superiority of tensor in terms of estimation performance due to an improved signal subspace estimate.

The rest of the thesis is organized as follows. In Chapter 2, the 3D system model used in this paper is described. Simplest separate estimation of channel parameters is introduced as preliminary work. In Chapter 3, we jointly estimate the elevation and azimuth angle using standard ESPRIT algorithm and then extend it into real processing domain by unitary transformation. Simulation results suggests that azimuth angle estimation performance is more vulnerable compared to elevation angle estimation. Impact of various antenna configurations onto estimation of MSE is investigated. In Chapter 4, we present the matrix-based 3D joint angle and delay estimation approach and its extension to 3D unitary ESPRIT algorithm. Furthermore, automatic pairing is achieved through a modified simultaneous Schur decomposition (SSD) [11]. We derive a tensor-based 3D JADE system model and naturally extends all the previous results for matrix case in Chapter 5. A detailed performance comparison between separate and joint estimation / matrix and tensor-based approach is given under various antenna configurations. It shows us how dimensionality and practical implementation will impact the channel estimation performance of a 2D antenna array at the base station. Finally, Chapter 6 concludes the thesis and we show a list of active research topics needed to be studied in the future.

Chapter 2

System Model

2.1 Channel Model Estimation

A typical 2D "Massive MIMO" system with an $M_1 \times M_2$ antenna array at the base station can be shown in Fig. 2.1 [12]. In this particular system, a base station is at the height of h while a

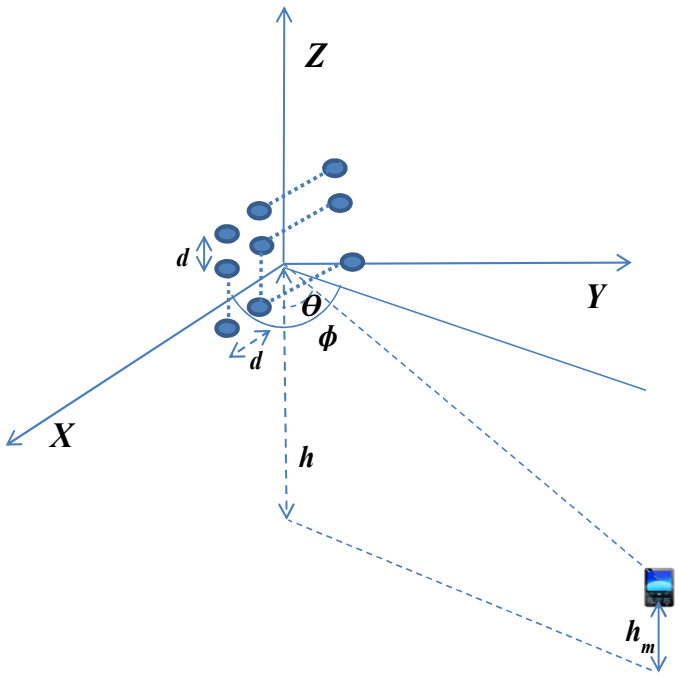

Figure 2.1: Model of 2D "Massive MIMO" System

mobile station is at the height of h_m. The antenna array at the base station is a planar array placed

in the X-Z domain with M_1 antenna elements vertically and M_2 antenna elements horizontally. The spacing between adjacent sensors is assumed to be d, without loss of generality, we fix it to the critical half wavelength distance in order to avoid the spatial spectrum alias. Since the matrix factorization form of the channel will get rather complicated for the case where both transmitter and receiver are equipped with multiple antennas. For simplicity, throughout this paper we assume that there is only one transmit antenna at the mobile station, which is also the typical scenario for modern cellular systems. Under this assumption, the transmit antenna array steering becomes a scalar which we normalize to 1. In the 2D "Massive MIMO" system, instead of mechanical down-tilting the antenna array towards the mobile station, the base station could also perform digital beamforming in both elevation and azimuth domain, because 2D DoA estimation will provide the base station some channel knowledge on the downlink.

In reality, the propagation situation in a wireless communication system is rather complicated. The uplink sounding reference signals usually go through scattering, reflection, refraction, and diffraction before they reach the base station. For a multi-path scenario, a wireless channel is usually modeled by a finite number of rays, each parameterized by a complex amplitude, spatial angle and time delay, *a.k.a* the multi-ray propagation model.

In this paper, we derive a data model for the reception of a single source in a multi-path scenario. Assume we transmit a digital sequence $\{s_k\}$ over a channel, and measure the response using $M_1 \times M_2$ antennas. The noiseless received data $Y(t)$ in general has the form

$$Y(t) = \sum_k s_k \, H(t - kT). \tag{2.1}$$

where T is the symbol rate and for notation simplicity, it will be normalized to $T = 1$ from now on. We writes the $M_1 \times M_2$ impulse response as

$$H(t) = \sum_{\ell=1}^{P} \alpha_\ell \, \mathbf{a}(u_\ell)\mathbf{a}^T(v_\ell) g(t - \tau_\ell). \tag{2.2}$$

where $g(t)$ is a known pulse shape function by which $\{s_k\}$ is modulated. In our scenario, there

are P distinct propagation paths and we assume the number P is available. Many of the signal detection methods are applicable to our model, e.g., the methods based on the AIC and MDL principle, since the path fading are normally distributed. Detailed performance comparison of these two criteria on model order statistics will be shown in Part II. α_ℓ denotes the complex envelope of the ℓ_{th} fading path. The vector-valued function $\mathbf{a}(u_\ell) = [1, e^{ju_\ell}, \cdots, e^{j(M_1-1)u_\ell}]^T$ and $\mathbf{a}(v_\ell) = [1, e^{jv_\ell}, \cdots, e^{j(M_2-1)v_\ell}]^T$ can be viewed as the steering vectors of elevation angle and azimuth angle respectively. $u_\ell = \frac{2\pi d}{\lambda}\cos\theta_\ell, v_\ell = \frac{2\pi d}{\lambda}\sin\theta_\ell\cos\phi_\ell$ represent two spatial frequencies of path ℓ according to our base station array configuration, λ is the wavelength.

Note that, our application is for wireless communication and the data model above indicates a broadband communication system. However, for further array signal processing, we need to make a narrowband phased array assumption. The narrowband signal and narrowband array are two different concepts, because the actual signal bandwidth alone cannot be used to categorize a signal as being narrowband or broadband. For different sensor arrays or even for different emitter locations relative to the array, the same signal may fall into either category. If B is the band width of the signal and $T_{\max}$ is the maximum time required by the signal to cross the array, then the situation below is considered as a narrowband array case

$$B \times T_{\max} \ \leq \ 1. \tag{2.3}$$

Obviously, this equation also depends upon the DoA and array geometry, therefore the same signal can be considered broadband or narrowband depending upon these parameters. Now, if we focus on azimuth domain, which is the general 1D uniform linear array case, we can find that as the direction of arrival angle approaches to 90, $T_{\max}$ approaches to 0 and when angle approaches to 0, $T_{\max}$ becomes larger. Moreover, $T_{\max}$ is also proportional to number of sensors in the array.

Since for broadband array scenario, the array steering vector will be frequency-dependent. In other words, if we assume a broadband antenna array, the delay between antenna elements cannot be approximately translated into phase shift in frequency domain, and no more Vandermonde

structure can be exploited. In this situation, the array manifold matrix varies significantly over the range of frequencies present and the ordinary signal-subspace approach fails. In particular, the spatial covariance matrix of the sensor output matrix generally has full rank, even for a single broadband signal. And this matrix cannot be used to define the signal subspace for the broadband case. Hence, we tackle this mobile communication problem under the narrowband array condition for the rest of the thesis.

Now, we need to stack dimensions through collecting all the array responses from an $M_1 \times M_2$ steering matrix $A(u_\ell, v_\ell) = \mathbf{a}(u_\ell)\mathbf{a}^T(v_\ell)$. To be specific, let $\mathbf{a}_\ell$ be the vector after the mapping of matrix $A(u_\ell, v_\ell)$, it can be shown that:

$$\mathbf{a}_\ell = \mathbf{a}(v_\ell) \otimes \mathbf{a}(u_\ell)$$

where $\otimes$ is the Kronecker product. From $\mathbf{a}_\ell$, we can construct a 2D steering matrix of the received signals, $A = [\mathbf{a}_1, \mathbf{a}_2, \ldots, \mathbf{a}_P] \in \mathcal{C}^{M_1 M_2 \times P}$, which contains all the information related to the P path signals whose elevation angle θ_ℓ and azimuth angle ϕ_ℓ are to be estimated.

It is reasonable to assume that the known modulation pulse shape function $g(t)$ has finite support $[0, L_g)$. With $\tau_{max} = \max\limits_{1 \le \ell \le P} \tau_\ell$ denotes the maximum delay spread, the channel length is $L = L_g + \tau_{max}$, which means the channel impulse response $\mathbf{h}(t)$ has finite duration and is zero outside an interval $[0, L)$ [13]:

$$\mathbf{h}(t) = \sum_{\ell=1}^{P} \alpha_\ell \, \mathbf{a}_\ell \, g(t - \tau_\ell) \tag{2.4}$$

where L and L_g are both measured in symbol periods. Thus the received data $Y(t)$ can be re-organized into an $M_1 M_2 \times 1$ vector $\mathbf{y}(t)$ for the time series data model. We assume that the received data is sampled at a rate of V times the symbol rate. Using either training sequences (known $\{s_k\}$) or blind channel estimation techniques, it is possible to estimate $\mathbf{h}(k)$, $k = 0, \frac{1}{P}, \cdots, L - \frac{1}{V}$, at least up to a scalar. Specifically, suppose we start sampling at $t = 0$ and collect samples of $\mathbf{y}(t)$ during

N symbol periods, the noiseless received data can be rewritten in compact form as

$$Y_v = H_v\, S \tag{2.5}$$

Herein,

$$Y_v = \begin{bmatrix} \mathbf{y}(0) & \mathbf{y}(1) & \cdots & \mathbf{y}(N-1) \\ \mathbf{y}(\frac{1}{V}) & \mathbf{y}(1+\frac{1}{V}) & \cdots & \mathbf{y}(N-1+\frac{1}{V}) \\ \vdots & \vdots & \ddots & \vdots \\ \mathbf{y}(1-\frac{1}{V}) & \mathbf{y}(2-\frac{1}{V}) & \cdots & \mathbf{y}(N-\frac{1}{V}) \end{bmatrix}$$

$$H_v = \begin{bmatrix} \mathbf{h}(0) & \mathbf{h}(1) & \cdots & \mathbf{h}(L-1) \\ \mathbf{h}(\frac{1}{V}) & \mathbf{h}(1+\frac{1}{V}) & \cdots & \mathbf{h}(L-1+\frac{1}{V}) \\ \vdots & \vdots & \ddots & \vdots \\ \mathbf{h}(1-\frac{1}{V}) & \mathbf{h}(2-\frac{1}{V}) & \cdots & \mathbf{h}(L-\frac{1}{V}) \end{bmatrix}.$$

$$S = \begin{bmatrix} s_0 & s_1 & \ddots & s_{N-1} \\ s_{-1} & s_0 & s_1 & \ddots \\ \ddots & \ddots & \ddots & \ddots \\ s_{-(L-1)} & s_{-(L-2)} & \cdots & s_{-(L-N)} \end{bmatrix}$$

where Y_v represents the $M_1M_2V \times N$ vectorized received data matrix while S is the $L \times N$ symbol matrix with Toeplitz structure. Note that, if transmitted sequence $\{s(k)\}$ is known for $k = -L+1, \cdots, N-1$ and $N \geq L$, we can directly estimate the $M_1M_2V \times L$ channel matrix through least-square type of methods and apply JADE algorithm, i.e., $\hat{H}_v = Y_v S^{\dagger}$, where the superscript $\dagger$ represents matrix pseudo-inverse.

It is convenient to rearrange the estimated impulse response samples into an $M_1M_2 \times LV$ channel matrix H_1 similarly as (2.4), including all the components: the array response, fading parame-

ters, symbol waveform and path delay:

$$H_1 = \begin{bmatrix} \mathbf{a}_1 & \cdots & \mathbf{a}_P \end{bmatrix} \begin{bmatrix} \alpha_1 & & \\ & \ddots & \\ & & \alpha_P \end{bmatrix} \begin{bmatrix} \mathbf{g}(\tau_1) \\ \vdots \\ \mathbf{g}(\tau_P) \end{bmatrix} \tag{2.6}$$

$$= ABG$$

where B is the $P \times P$ diagonal matrix containing complex fading envelope. G denotes the $P \times LV$ time delay matrix, where $\mathbf{g}(\tau_\ell) = [g(k-\tau_\ell)]_{k=0,1/V,\cdots,L-1/V}$ is a $1 \times LV$ row vector of samples of $g(t-\tau_\ell)$. At this point, we can easily solve the joint azimuth-elevation estimation problem using 2D ESPRIT techniques [12], as long as we have the channel estimate. We will discuss it in more detail within chapter 3.

2.2 ESPRIT-based Delay Estimation

In this section, we will introduce the delay estimation algorithm using shift-invariance structure, by the fact that a Fourier transform maps a delay to phase progression. Usually, the pulse shaping function $g(t)$ is assumed to be raised cosine roll-off signal because of its capability in reducing inter symbol interference (ISI) from multi-path signal reflections. As in our model, the known transmitted waveform $g(t)$ is sampled at a rate of V times and we denote the $1 \times LV$ row vector as:

$$\mathbf{g} = [g(0), g(\tfrac{1}{V}), \cdots g(L-\tfrac{1}{V})] \tag{2.7}$$

Here, we use a discrete Fourier transform (DFT) to the samples of time sequence as $\mathbf{G}_F = \mathbf{g}\, F_{DFT}$, where F_{DFT} represents the DFT matrix of size $LV \times LV$.

$$\mathbf{G}_F = \mathbf{g}\, F_{DFT} = \mathbf{g} \begin{bmatrix} 1 & 1 & \cdots & 1 \\ 1 & \Phi & \cdots & \Phi^{(LV-1)} \\ \vdots & \vdots & \ddots & \vdots \\ 1 & \Phi^{(LV-1)} & \cdots & \Phi^{(LV-1)^2} \end{bmatrix}, \quad \Phi = e^{-j\frac{2\pi}{LV}}$$

Obviously, if τ_ℓ is an integer multiple of $\frac{1}{V}$, we can directly obtain:

$$\mathbf{G}_F(\tau_\ell) = [1, \Phi^{\tau_\ell V}, \Phi^{2\tau_\ell V}, \cdots, \Phi^{(LV-1)\tau_\ell V}]\ \mathrm{diag}[\mathbf{G}_F]$$

Note that, this equation holds true for any τ if $g(t)$ is bandlimited and sampled at or above the Nyquist rate, and these two inherent assumptions are reasonable to make in most circumstances within digital communication area. The channel matrix in (2.6) after DFT transformation

$$H_F = H_1\, F_{DFT}$$

can be shown as:

$$\begin{aligned} H_F &= AB \begin{bmatrix} 1 & \psi_1 & \cdots & \psi_1^{LV-1} \\ 1 & \psi_2 & \cdots & \psi_2^{LV-1} \\ \vdots & \vdots & \vdots & \vdots \\ 1 & \psi_P & \cdots & \psi_P^{LV-1} \end{bmatrix} \mathrm{diag}(\mathbf{G}_F) \\ &= ABF\,\mathrm{diag}(\mathbf{G}_F) \end{aligned}$$

where $\psi_\ell = e^{-j\frac{2\pi}{L}\tau_\ell}, \ell = 1, 2, \cdots, P$. From the above equation, it is clear that the phase shift matrix F is a Vandermonde matrix, which reminds us of the ESPRIT algorithm. If the matrix $\mathrm{diag}(\mathbf{G}_F)$ is

nonsingular, we can have:

$$\hat{H}_F = H_F \cdot \{\mathrm{diag}(\mathbf{G}_F)\}^{-1} = ABF \tag{2.8}$$

In order to apply the standard ESPRIT algorithm, we should transpose the above channel model $\hat{H}_F$ to reverse the matrices multiplication order. Let F_ψ denote the transposed time delay matrix, we can obtain:

$$H_\tau = (\hat{H}_F)^T = F_\psi (AB)^T . \tag{2.9}$$

Note that, the role of F_ψ equals to the array steering matrix in our former data model [12], which means the delay estimation problem has been transformed to a typical DoA estimation problem. If the number of multi-paths is not larger than the number of antennas (e.g., $P \leq M_1$ and $P \leq M_2$), then we can follow our line of work to obtain ψ_ℓ, as well as the parameter of interest τ_ℓ through shift-invariance property of the transposed channel matrix H_τ, independent of the structure of A. However, in general, the number of antennas is limited and might not satisfy the condition ($P > M_1$ and $P > M_2$). This problem can be avoided by constructing a Hankel matrix out of $\hat{H}_F$, and we will explain more in section 4.1 of chapter 4. By this mean, we can have various antenna configurations even for two antenna elements on one direction.

From equation (2.8) and (2.9) it is clear that the angles and delay can be estimated independently of each other, by directly working on the rows and columns of the transformed channel matrix H_τ. However, this does not give a pairing between angles and the corresponding delay, and might result in poor resolution for closely spaced angles and delays. We will introduce the 3D joint angle and delay estimation algorithm for rectangular planar array in chapter 4.

Chapter 3

2D Joint DoA Estimation

3.1 2D DoA Estimation Data Model

For simplicity and comparison purpose, we first settle 2D joint angle estimation problem before we approach the 3D joint one. All system settings remain the same except for the absence of delay, thus we simply rewrite the channel matrix as:

$$H_a = \sum_{\ell=1}^{P} \alpha_\ell \, \mathbf{a}(u_\ell)\mathbf{a}^T(v_\ell) \tag{3.1}$$

Alternatively, we can use center of the antenna array as reference point because conjugate symmetry property can significantly reduce the computational complexity, but it won't make any difference to our subsequent algorithm procedure.

From (3.1), it can be seen that for the case where there is only one transmit antenna at the mobile station the uplink channel completely depends on the DoA at the base station array. In time-division-duplex (TDD) systems, there exists a reciprocity property between uplink channel and the downlink channel. Therefore, the base station could potentially conduct downlink MIMO operations for 2D "massive MIMO" systems based on the DoA estimation from the uplink. This is also the reason why DoA estimation is critical for 2D "massive MIMO" systems.

Similarly, after vectorization, the channel matrix now is a $M_1M_2 \times P$ matrix, denoted by H_{av}.

Accordingly, the $M_1M_2 \times K$ received data matrix Y_{av} (after the vector mapping) for K snapshots can be written as

$$Y_{av} = H_{av}S_a + N_{av},$$

where $S_a = [s_1, s_2, \ldots, s_P]^T$ are the $P \times K$ transmitted signals at the mobile device, and $s_\ell = [s_{\ell 1}, s_{\ell 2}, \ldots, s_{\ell K}]$. Here the signals $s_1, s_2, \ldots, s_P$ should be the same for our single source multi-path scenario. N_{av} denotes the vectorized $M_1M_2 \times K$ AWGN noise matrix, with noise power σ_n^2 at each receiver antenna element. Note that after rearranging the received signals into the steering matrix form, the system model of the 2D antenna array is exactly the same as that of the 1D antenna array.

Using the standard estimation of signal parameters via rotational invariance techniques (ESPRIT) algorithm [14], a common model with shift invariance property can be given by

$$A_0\Phi = A_1,$$

where A_0 stands for the first $M_2 - 1$ rows and A_1 stands for the last $M_2 - 1$ rows of the M_1 blocks of the transposed steering matrix A (aiming to estimate spatial frequency v_ℓ first). Φ is a diagonal matrix whose entries are the phase shift of adjacent elements horizontally. Let U_s be the $MN \times P$ matrix of signal eigenvectors. Since the steering vectors in matrix A span the same subspace as U_s, there exists an invertible matrix T such that $U_s = AT$. Constructing matrices U_{s0} and U_{s1} from U_s as A_0 and A_1 from A, and let the transition matrix $\Psi = T^{-1}\Phi T$, we have

$$U_{s1} = U_{s0}\Psi. \tag{3.2}$$

Note that the matrix Φ is a diagonal matrix containing the eigenvalues of Ψ. Using total least square method, we will be able to solve equation (3.2) to obtain the estimated spatial frequencies of v_ℓ and similar to the spatial frequencies of u_ℓ. In 2D "massive MIMO" systems, the two spatial frequencies u_ℓ and v_ℓ in the steering matrix are related to the elevation and azimuth angles of incoming signals we are interested in. There are many existing methods, especially subspace-

fitting based, to estimate the 2D DoA corresponding to this typical system model, e.g., MUSIC, matrix pencil and ESPRIT. However, the computational complexity of these original algorithms is prohibitively high.

3.2 Low Complexity 2D DoA Estimation

In this section, we will introduce a low complexity approach based on unitary ESPRIT algorithm to jointly estimate the elevation and azimuth angles. The unitary transformation (*a.k.a.* real processing) will convert complex matrices to real matrices, and all subsequent operations to the real domain, with obvious computational and numerical advantages.

As discussed in section 2.1, the array manifold matrix of an $M_1 \times M_2$ antenna array can be expressed as $A(u_\ell, v_\ell) = \mathbf{a}(u_\ell)\mathbf{a}^T(v_\ell)$, that is, the 2D steering matrix can be decomposed to the product of two 1D steering vectors.

For $\mathbf{a}(u_i)$, if the first $(M_1 - 1)$ elements are multiplied by e^{ju_ℓ} , the resulting vector will be equal to the last $(M_1 - 1)$ components. This can be expressed as:

$$e^{ju_\ell} J_1 \mathbf{a}(u_\ell) = J_2 \mathbf{a}(u_\ell) \tag{3.3}$$

where J_1 is an $(M_1 - 1) \times M_1$ matrix constructed by taking the first $(M_1 - 1)$ rows of I_{M_1} ($M_1 \times M_1$ identity matrix) and J_2 is the $(M_1 - 1) \times M_1$ matrix constructed by taking the last$(M_1 - 1)$ rows of I_{M_1}. A unitary matrix, Q_{M_1}, can be constructed to change the steering vector to real values. That is,

$$\mathbf{a}^R(u_\ell) = Q_{M_1}^H \mathbf{a}(u_\ell),$$

Assuming $M_1 = 2q$ which is an even number, Q_{M_1} can be constructed as

$$Q_{2K} = \frac{1}{\sqrt{2}} \begin{bmatrix} I_q & jI_q \\ \Pi_q & j\Pi_q \end{bmatrix},$$

where I_q is the $q \times q$ unit matrix, and Π_M is the $M \times M$ exchange matrix with ones on the anti-diagonal and zeros elsewhere. Since Q_{M_1} is unitary, we can rewrite (3.3) as

$$e^{ju_\ell} J_1 Q_{M_1} Q_{M_1}^H \mathbf{a}(u_\ell) = J_2 Q_{M_1} Q_{M_1}^H \mathbf{a}(u_\ell). \tag{3.4}$$

Multiplying $Q_{M_1-1}^H$ on both sides gives us

$$e^{ju_\ell} Q_{M_1-1}^H J_1 Q_{M_1} \mathbf{a}^R(u_\ell) = Q_{M_1-1}^H J_2 Q_{M_1} \mathbf{a}^R(u_\ell). \tag{3.5}$$

It can be shown that $Q_{M_1-1}^H J_2 Q_{M_1} = \left(Q_{M_1-1}^H J_1 Q_{M_1} \right)^*$. Let $K_1 = \mathrm{Re}\left\{ Q_{M_1-1}^H J_2 Q_{M_1} \right\}$, and $K_2 = \mathrm{Im}\left\{ Q_{M_1-1}^H J_2 Q_{M_1} \right\}$. We can have the following relation:

$$\tan\left(\frac{u_\ell}{2}\right) K_1 \mathbf{a}^R(u_\ell) = K_2 \mathbf{a}^R(u_\ell) \tag{3.6}$$

We can extend the relation to 2D antenna array

$$\tan\left(\frac{u_\ell}{2}\right) K_1 A^R(u_\ell, v_\ell) = K_2 A^R(u_\ell, v_\ell), \tag{3.7}$$

where

$$A^R(u_\ell, v_\ell) = Q_{M_1}^H \mathbf{a}(u_\ell) \mathbf{a}^T(v_\ell) Q_{M_2}^* = \mathbf{a}^R(u_\ell) (\mathbf{a}^R(v_\ell))^T.$$

Let $\mathrm{vec}\{\cdot\}$ be the vector operation, we can rewrite the formulation in (3.7) as

$$\tan\left(\frac{u_\ell}{2}\right) K_{x1} \mathrm{vec}\left\{ A^R(u_\ell, v_\ell) \right\} = K_{x2} \mathrm{vec}\left\{ A^R(u_\ell, v_\ell) \right\}$$

where $K_{x1} \triangleq I_{M_2} \otimes K_1$, and $K_{x2} \triangleq I_{M_2} \otimes K_2$. Accordingly, we can specify an $M_1 M_2 \times P$ real array manifold matrix:

$$A^R \triangleq \left[\mathrm{vec}\left\{ \mathbf{a}^R(u_1, v_1) \right\}, \ldots, \mathrm{vec}\left\{ \mathbf{a}^R(u_P, v_P) \right\} \right]$$

Accordingly, we have

$$K_{x1}A^R\Omega_x = K_{x2}A^R \tag{3.8}$$

where

$$\Omega_x \triangleq \text{diag}\left\{\tan\left(\frac{u_1}{2}\right), \tan\left(\frac{u_2}{2}\right), \ldots, \tan\left(\frac{u_P}{2}\right)\right\}$$

It is important to note that after the unitary transformation, the matrices become real matrices. Hence, all the subsequent operations turn to be real processing. This will significantly reduce the computational complexity.

Similarly, for $\mathbf{a}(v_\ell)$, we can conduct the same process. Let $K_3 = \text{Re}\left\{Q^H_{M_2-1}J_2'Q_{M_2}\right\}$, and $K_4 = \text{Im}\left\{Q^H_{M_2-1}J_2'Q_{M_2}\right\}$, where J_2' is the $(M_2-1)\times M_2$ matrix constructed by taking the last (M_2-1) rows of I_{M_2}. Accordingly, we have

$$K_{y1}A^R\Omega_y = K_{y2}A^R \tag{3.9}$$

where $K_{y1} \triangleq K_3 \otimes I_{M_1}$, $K_{y2} \triangleq K_4 \otimes I_{M_1}$, and

$$\Omega_y \triangleq \text{diag}\left\{\tan\left(\frac{v_1}{2}\right), \tan\left(\frac{v_2}{2}\right), \ldots, \tan\left(\frac{v_P}{2}\right)\right\} \tag{3.10}$$

Let U_s be the signal subspace and T be the linear transformation matrix. Since the signal subspace and the steering vector spans the same subspace, we have $U_s = A^R T$. Substituting this relation into (3.8), we have

$$K_{x1}U_s\Upsilon_x = K_{x2}U_s \tag{3.11}$$

where $\Upsilon_x \triangleq T^{-1}\Omega_x T$. Similarly, we can also have

$$K_{y1}U_s\Upsilon_y = K_{y2}U_s \tag{3.12}$$

where $\Upsilon_y \triangleq T^{-1}\Omega_y T$.

From (3.11) and (3.12), we can solve for $\hat{\Upsilon}_x$ and $\hat{\Upsilon}_y$ based on the estimated signal subspace $\hat{U}_s$.

Let the eigenvalues of the $P \times P$ complex matrix $\hat{\Upsilon}_x + j\hat{\Upsilon}_y$ be $\hat{\lambda}_\ell, \ell = 1,2,\ldots,P$. Accordingly, u_ℓ and v_ℓ can be estimated from

$$\hat{u}_\ell = 2\tan^{-1}\left\{\mathrm{Re}\left(\hat{\lambda}_\ell\right)\right\}$$

$$\hat{v}_\ell = 2\tan^{-1}\left\{\mathrm{Im}\left(\hat{\lambda}_\ell\right)\right\}$$

where 2D DoAs of interest will be obtained through simple parameter transformation. The 2D unitary ESPRIT algorithm can be summarized as:

1. Estimate $\hat{U}_s$ from the received signals.
2. Compute $\hat{\Upsilon}_x$ and $\hat{\Upsilon}_y$.
3. Compute the eigenvalues $\hat{\lambda}_\ell, \ell = 1,2,\ldots,P$.
4. Compute u_ℓ and v_ℓ.
5. Compute $\hat{\theta}_\ell$ and $\hat{\phi}_\ell$ from u_ℓ and v_ℓ.

In order to evaluate the estimation performance, we assume a two paths situation with DoAs $[70,77]^\circ$ for elevation and $[45,60]^\circ$ for azimuth angle, path fading amplitudes $[1,0.8]$ and time delay $[0.5,2.1]$, respectively. The known pulse shape function we use is a raised cosine signal, with roll-off factor 0.3 and oversampling rate 2 compared to the normalized symbol rate. The number of snapshots at each array element is 1000.

The performance of joint DoA estimation based on unitary ESPRIT under SNR, ranging form -6 dB to 24 dB (dynamic range of SNR in a cellular environment), is evaluated in Fig. 3.1 and Fig. 3.2 under various antenna configurations. The MSE we defined here is the difference between angles in degree. We can see from Fig. 3.1 that the elevation angle estimation performance of different antenna structures are almost parallel to each other, also the MSE decreases as the SNR increases. However, it is interesting to note that the estimation performance of azimuth angle doesn't scale proportionally to the number of antennas horizontally, as shown in Fig. 3.2. We observe that the MSE of azimuth estimation of a 2×32 array is even larger than that of 4×16, which

seems a little bit counter-intuitive. The reason for this phenomenon to happen is because azimuth estimation is actually coupled with elevation estimation. In the case of 2×32 antenna configuration, the performance of elevation is so poor that it affects the performance of azimuth estimation.

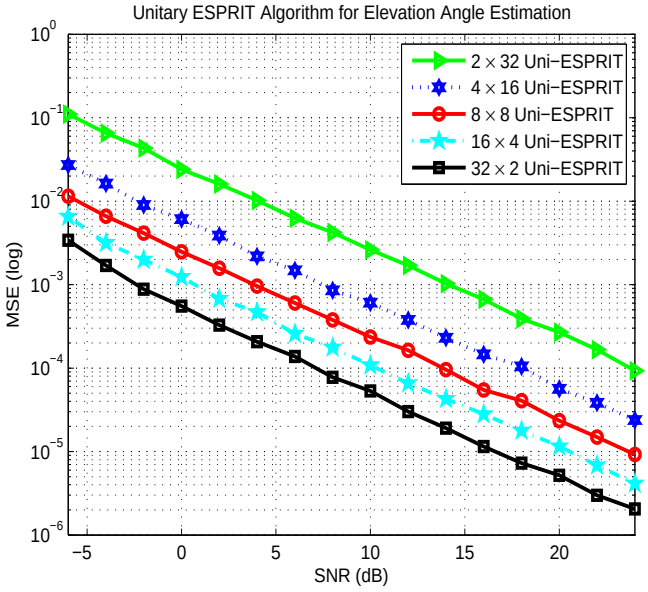

Figure 3.1: Unitary Joint Elevation Angle Estimation

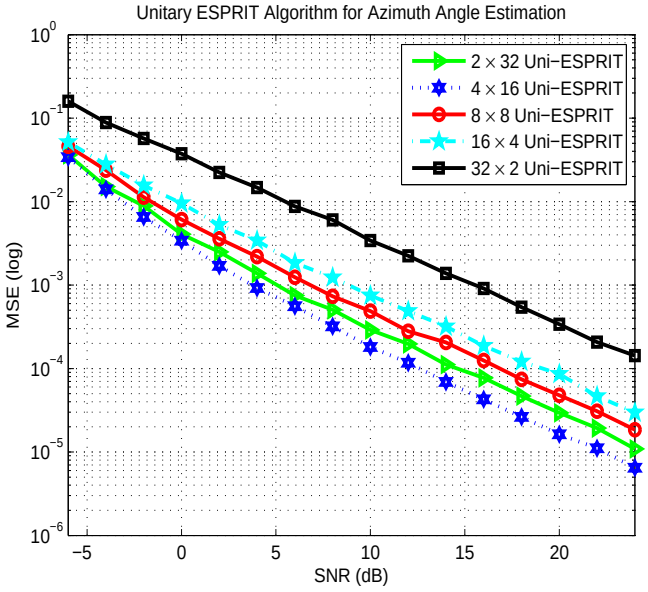

Figure 3.2: Unitary Joint Azimuth Angle Estimation

While for delay estimation, the simulation assumptions remain the same, its performance is shown

in Fig. 3.3. We can see from the figure that the low complexity algorithm gives out a quite accurate estimate of path delay. The MSE reduces as SNR increases, and different antenna configurations have no impact to the estimation performance. This result is not surprising since we can see it from the Fisher Information Matrix derived in [12]. The performance depends on the total number of antenna elements (e.g., in our case, $N_r = M_1 M_2$) rather than the various configurations. Note that, once the total number of antenna elements is fixed, the estimation accuracy of delay only depends on the DFT matrix given in (2.7). Furthermore, same phenomenon exists for the Cramer-Rao lower bounds on joint angle estimation and delay estimation in section IV of [12].

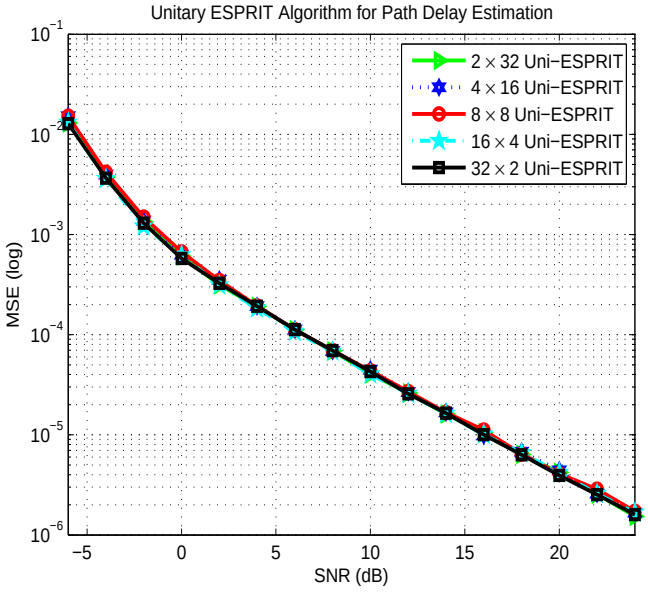

Figure 3.3: Unitary Separate Delay Estimation

Chapter 4

Joint Angle and Delay Estimation

In this chapter, we will construct a space-time manifold matrix through stacking data into a Hankel matrix and jointly estimate the delay and DoAs using 3D ESPRIT-like algorithm. While for next chapter, a tensor-based system model will come into picture such that an improved signal subspace estimate is available. Extension to real processing and auto-pairing is straightforward, and we will illustrate them in section 4.2. Further analysis and simulation results of the estimation performance are given in section 5.3 in chapter 5.

4.1 Matrix-based Joint Estimation Using Standard ESPRIT

Recall section 2.2 that, the most advantage of JADE is that it can work even when the number of multi-paths exceeds the number of antennas, as long as the space-time manifold is a tall matrix. This can be done through constructing a Hankel matrix by left-shifting and stacking M_3 copies of $\hat{H}_F$ to satisfy the requirement [13]. In particular, for a $1 \leq i \leq M_3$, define the left-shifted matrix $\hat{H}_F{}^{(i)} \triangleq \hat{H}_{F\,(:,\ i:LV-M_3+i)}$. (The notation $_{(:,\ i:LV-M_3+i)}$ indicates taking columns i through $LV-M_3+i$ of a matrix). Then we define the 3D stacked tall channel matrix $\mathbf{H}$, which involves delay, elevation

angle and azimuth angle as:

$$\mathbf{H} \triangleq \begin{bmatrix} \hat{H_F}^{(1)} \\ \hat{H_F}^{(2)} \\ \vdots \\ \hat{H_F}^{(M_3)} \end{bmatrix} \quad (\text{Its dimension is } M_3M_1M_2 \times LV - M_3 + 1)$$

The reason why we construct the big matrix in this structure is because $\mathbf{H}$ has a factorization as

$$\mathbf{H} = \mathbf{A}BF, \quad \mathbf{A} \triangleq \begin{bmatrix} A \\ A\Psi \\ \vdots \\ A\Psi^{(M_3-1)} \end{bmatrix} = A_\psi \diamond A \triangleq \begin{bmatrix} 1 & 1 & \cdots & 1 \\ \psi_1 & \psi_2 & \cdots & \psi_P \\ \vdots & \vdots & \vdots & \vdots \\ \psi_1^{M_3-1} & \psi_2^{M_3-1} & \cdots & \psi_P^{M_3-1} \end{bmatrix} \diamond A$$

Here, A_ψ represents the virtual time delay matrix, and $\mathbf{A}(\tau,\theta,\phi) = A_\psi \diamond A$ is the space-time manifold matrix. Both A_ψ and A are with Vandermonde structure. $\diamond$ denotes the Khatri-Rao product, i.e., a column-wise Kronecker product. Note that, the array manifold for elevation angle estimation is different from azimuth angle estimation, whose relationship is transpose of each other, $\mathbf{A}(\tau,\phi,\theta) = A_\psi \diamond A_t$, where $A_{t\ell} = \mathbf{a}(u_\ell) \otimes \mathbf{a}(v_\ell)$. If we can choose the stacking parameter w such that both $M_3M_1M_2 \geq P$ and $LV - M_3 + 1 \geq P$ are satisfied, and if all factors are full rank, then $\mathbf{H}$ has rank P, which means that we can estimate $\mathbf{A}$ up to a $P \times P$ factor matrix at the right. Hence, after proper vectorization and utilization of the shift-invariance property of this highly structured matrix, we can jointly estimate the unknowns based on standard ESPRIT-like algorithms.

To estimate ψ_ℓ, we should take the first and respectively last $M_1M_2(M_3-1)$ rows of channel matrix as two submatrices, while for θ_ℓ estimation, we may take its first and respectively last $M_1 - 1$ rows for all M_3M_2 blocks of channel matrix, similarly, for ϕ_ℓ estimation, we may take its first and respectively last $M_2 - 1$ rows for all M_3M_1 blocks. Hence, we can define the selection matrices as

follows:

$$J_{1\psi} = [I_{M_3-1}\ 0_1] \otimes I_{M_1M_2} \quad J_{2\psi} = [0_1\ I_{M_3-1}] \otimes I_{M_1M_2}$$
$$J_{1\theta} = I_{M_3M_2} \otimes [I_{M_1-1}\ 0_1] \quad J_{2\theta} = I_{M_3M_2} \otimes [0_1\ I_{M_1-1}]$$
$$J_{1\phi} = I_{M_3M_1} \otimes [I_{M_2-1}\ 0_1] \quad J_{2\phi} = I_{M_3M_1} \otimes [0_1\ I_{M_2-1}]$$

Through shift-invariance property, we can write:

$$\begin{aligned} H_{1\psi} &= A_\psi BF \quad H_{2\psi} = A_\psi \Psi BF \\ H_{1\theta} &= A_\theta BF \quad H_{2\theta} = A_\theta \Theta BF \\ H_{1\phi} &= A_\phi BF \quad H_{2\phi} = A_\phi \Phi BF, \end{aligned} \tag{4.1}$$

where Ψ, Θ and Φ are the corresponding diagonal matrices, containing desired parameters for each path, $\Psi = \text{diag}[\psi_1, \ldots, \psi_P]$, $\Theta = \text{diag}[\theta_1, \ldots, \theta_P]$ and $\Phi = \text{diag}[\phi_1, \ldots, \phi_P]$. Here, $H_{1\psi} = J_{1\psi}\mathbf{H}$ and $A_\psi = J_{1\psi}\mathbf{A}(\tau, \theta, \phi)$, other matrices are similarly defined.

After stacking the data into a Hankel matrix, we have sufficient "information" to make ESPRIT algorithm work with respect to the available antenna array elements. Then we can directly apply the 3D ESPRIT-like algorithm [15] to jointly estimate the delay and 2D DoAs if dimensions are such that these are low-rank factorizations. However, we still need to have them correctly paired before the result is finalized. Several issues are involved with automatic-pairing and will be described in next subsection.

4.2 Real processing and Automatic-pairing

For practical multi-path situation, we always use forward-backward averaging (FBA) as a pre-processing step in order to enhance the estimation accuracy. The main requirement for FBA to be valid is that the properties of the process under consideration be approximately the same independent of the orientation of the time or space axis and that the samples be taken in a geometry that is also reversible. Here, we have this property already by the assumption of using ESPRIT algo-

rithm, the antenna array at the base station is centro-symmetric. When FBA is possible, it yields an effective doubling of the data along with the expected improvements in estimator variances. Furthermore, in DoA applications, FBA has the desirable effect of reducing correlation between multi-path coherent signals. Lastly, if FBA is using, the spatial covariance matrix can efficiently be transformed into a real-valued matrix, which significantly reduces the computational complexity of the subsequent signal subspace estimation step. If such a transformation is used for unitary ESPRIT, real-valued computations can be maintained for all steps of the algorithm. Actually, FBA and unitary ESPRIT are naturally integrated.

Hence, for the rest of this section, we will first extend the low complexity Unitary ESPRIT algorithm to 3D case. Then FBA will be applied. In the end, we will mainly talk about auto-pairing using joint diagonalization with simultaneous Schur decomposition.

4.2.1 3D extension of Unitary ESPRIT

In section 3.2, we have outlined 2D unitary ESPRIT algorithm for joint elevation and azimuth angle estimation. Here, we will extend it to 3D case in a similar fashion. By now, we already have the steering vectors and selection matrices ready. Note that, the third dimension indicating delay shares the same exponential form as the other two spatial frequencies, described as $\mathbf{a}(\varpi_\ell) = [1, e^{j\psi_\ell}, \cdots, e^{j(M_3-1)\psi_\ell}]^T$, where $\psi_\ell = e^{-j\frac{2\pi}{L}\tau_\ell}, \ell = 1,2,\cdots,P$.

Similarly, we need to construct three unitary matrices $Q_{m_1}, Q_{m_2} and Q_{m_3}$ to change the steering vectors to real values. For elevation, azimuth and delay, the corresponding dimension of upper sub-matrices are:

$$m_1 = M_1 M_2 (M_3 - 1)$$

$$m_2 = (M_1 - 1) M_2 M_3$$

$$m_3 = M_1 (M_2 - 1) M_3$$

Assuming $m_1 = 2q_1, m_2 = 2q_2$ and $m_3 = 2q_3$ which are all even numbers, we have

$$Q_{m_1} = \frac{1}{\sqrt{2}} \begin{bmatrix} I_{q_1} & jI_{q_1} \\ \Pi_{q_1} & j\Pi_{q_1} \end{bmatrix}, Q_{m_2} = \frac{1}{\sqrt{2}} \begin{bmatrix} I_{q_2} & jI_{q_2} \\ \Pi_{q_2} & j\Pi_{q_2} \end{bmatrix}, Q_{m_3} = \frac{1}{\sqrt{2}} \begin{bmatrix} I_{q_3} & jI_{q_3} \\ \Pi_{q_3} & j\Pi_{q_3} \end{bmatrix},$$

Furthermore, the right unitary matrix Q_{N_r}, where $N_r = M_1 M_2 M_3 \triangleq 2M$ is defined as

$$Q_{N_r} = \frac{1}{\sqrt{2}} \begin{bmatrix} I_M & jI_M \\ \Pi_M & j\Pi_M \end{bmatrix},$$

As in the 2D case in section 3.2, let us define the transformed steering matrix as $\mathbf{A}^R = Q_{N_r}^H \mathbf{A}$. Based on the three invariance properties of the multi-dimensional steering matrix $\mathbf{A}$, it is straightforward to get the transformed equation as:

$$\begin{aligned} K_{1\psi}\mathbf{A}^R \cdot \Omega_\psi &= K_{2\psi}\mathbf{A}^R \\ K_{1\theta}\mathbf{A}^R \cdot \Omega_\theta &= K_{2\theta}\mathbf{A}^R \\ K_{1\phi}\mathbf{A}^R \cdot \Omega_\phi &= K_{2\phi}\mathbf{A}^R \end{aligned} \tag{4.2}$$

where the three corresponding pairs of transformed selection matrices are given by:

$$\begin{aligned} K_{1\psi} &= 2 \cdot \mathrm{Re}\{Q_{m_1}^H J_{2\psi} Q_{N_r}\} \quad & K_{2\psi} &= 2 \cdot \mathrm{Im}\{Q_{m_1}^H J_{2\psi} Q_{N_r}\} \\ K_{1\theta} &= 2 \cdot \mathrm{Re}\{Q_{m_2}^H J_{2\theta} Q_{N_r}\} \quad & K_{2\theta} &= 2 \cdot \mathrm{Im}\{Q_{m_2}^H J_{2\theta} Q_{N_r}\} \\ K_{1\phi} &= 2 \cdot \mathrm{Re}\{Q_{m_3}^H J_{2\phi} Q_{N_r}\} \quad & K_{2\phi} &= 2 \cdot \mathrm{Im}\{Q_{m_3}^H J_{2\phi} Q_{N_r}\} \end{aligned}$$

and the three real-valued diagonal matrices

$$\begin{aligned} \Omega_\psi &\triangleq \mathrm{diag}\left\{\tan\left(\frac{\varpi_1}{2}\right), \tan\left(\frac{\varpi_2}{2}\right), \ldots, \tan\left(\frac{\varpi_P}{2}\right)\right\} \\ \Omega_\theta &\triangleq \mathrm{diag}\left\{\tan\left(\frac{u_1}{2}\right), \tan\left(\frac{u_2}{2}\right), \ldots, \tan\left(\frac{u_P}{2}\right)\right\} \\ \Omega_\phi &\triangleq \mathrm{diag}\left\{\tan\left(\frac{v_1}{2}\right), \tan\left(\frac{v_2}{2}\right), \ldots, \tan\left(\frac{v_P}{2}\right)\right\} \end{aligned}$$

contain the desired "spatial frequency" information. Till now, all the real-transformation for steering vectors and construction of selection matrices are complete. In order to keep the SVD of channel data matrix and all subsequent operations in the real domain, forward-backward averaging comes into the picture.

4.2.2 Forward-Backward Averaging

Since we are exploiting the specific eigenstructure properties of the sensor array output covariance matrix, it is natural to combine FBA into unitary ESPRIT framework. We use the fact that the eigenvalues are on the unit circle, along wit the symmetric structures of A_ψ, A_θ and A_ϕ. Let Π_{N_r} denote the exchange matrix which reverses the ordering of rows and Π_{N_c} denotes which reverses the ordering of the columns, and define

$$\mathbf{H}_{\mathrm{FB}} = [\mathbf{H} \quad \Pi_{N_r}\, \bar{\mathbf{H}}\, \Pi_{N_c}]$$

Here, $\bar{}$ indicates complex conjugate. In our later simulation, we set the number of paths P to two since forward-backward averaging can only resolve up to two paths. If we want to resolve more paths, spatial smoothing technique should be taken into account. Spatial smoothing pre-processing step leads to a decorrelation of the paths and an increase in the number of available snapshots. The key idea is that we divide the array into a number of identical displaced sub-arrays and average the spatial covariance matrix over these sub-arrays. Consequently, array aperture is sacriced. Haardt et al. [16] already incorporated spatial smoothing technique to unitary ESPRIT both in matrix and tensor form, more details can be seen in section VI of [16].

Then we multiply unitary matrices on both sides of $\mathbf{H}_{\mathrm{FB}}$ to transform the complex-valued data matrix into real-valued domain.

$$\mathbf{HH} = Q_{N_r}\, \mathbf{H}_{\mathrm{FB}}\, Q_{N_N} \qquad (\text{Its Dimension: } M_1 M_2 M_3 \times N_N)$$

where we assume $N_N = 2N_c = 2(LV-1)$ and

$$Q_{N_N} = \frac{1}{\sqrt{2}} \begin{bmatrix} I_{N_c} & jI_{N_c} \\ \Pi_{N_c} & j\Pi_{N_c} \end{bmatrix},$$

Similarly, we have $U_s \in \mathbb{R}^{M_1M_2M_3 \times P}$ the signal subspace from a real-valued SVD of $\mathbf{HH}$ and T be the linear nonsingular transformation matrix (whose dimension is $P \times P$). Since the signal subspace and the real-valued steering matrix $\mathbf{A}^R$ spans the same $P-$ dimensional subspace asymptotically or under the case of no additive noise, we have $U_s \approx \mathbf{A}^R T$. Substituting this relation into (4.2), we have three real-valued invariance equations:

$$\begin{aligned} K_{1\psi}U_s \cdot \Upsilon_\psi &= K_{2\psi}U_s \\ K_{1\theta}U_s \cdot \Upsilon_\theta &= K_{2\theta}U_s \\ K_{1\phi}U_s \cdot \Upsilon_\phi &= K_{2\phi}U_s \end{aligned} \tag{4.3}$$

where $\Upsilon_\psi \triangleq T^{-1}\Omega_\psi T$, $\Upsilon_\theta \triangleq T^{-1}\Omega_\theta T$ and $\Upsilon_\phi \triangleq T^{-1}\Omega_\phi T$. Here, the three real-valued matrices Υ_ψ, Υ_θ and Υ_ϕ are related with the diagonal matrices via eigenvalue preserving similarity transformations. Moreover, they share the same set of eigenvectors T in the noiseless case or with an infinite number of experiments. The problem now is if these eigenvalue solutions were calculated independently via LS, TLS or SLS, it would be quite difficult to pair the resulting three distinct sets of spatial frequency estimates. An easy way to make sure automatic pairing is to find the matrix of eigenvectors T the same for all three dimensions.

However, in practice, we only have a finite number of noise-corrupted snapshots. Therefore, the three real-valued matrices Υ_ψ, Υ_θ and Υ_ϕ do not exactly share the same set of eigenvectors. If we just choose one dimension to determine the set of common eigenvectors, the solution will rely on this specific choice and discard information contained in other two matrices. Obviously, it is not the best option. Thus, from a statistical point of view, it is desirable, for the sake of accuracy and robustness, to compute the "average eigenstructure" of these three matrices. In the 2D

case, we solve this problem by a trick, which is to calculate the eigenvalues of the "complexified" matrix $\hat{\Upsilon}_x + j\hat{\Upsilon}_y \in \mathbb{C}^{P\times P}$, kind of averaging. Therefore, automatic pairing of the eigenvalues can be achieved. However, for 3D case, this trick doesn't work anymore and we develop a Jacobi-type method to calculate an SSD of several nonsymmetric matrices. Note that, this method also extends to multi-dimensional case.

4.2.3 Joint diagonalization

Recall that the real eigenvalues of real-valued nonsymmetric matrices can efficiently be computed through an eigenvalue revealing real Schur decomposition. In the noiseless case or with an infinite number of experiments, the SSD of the three matrices Υ_ψ, Υ_θ and Υ_ϕ yields three real-valued upper triangular matrices that exhibit the automatically paired eigenvalues on their main diagonals. Under the assumption of additive noise and a finite number of experiments, an orthogonal similarity transformation might not be able to produce three upper triangular matrices simultaneously, since the three noisy matrices do not share a common set of eigenvectors. In this case, the resulting matrices should be "almost" upper triangular in a least square sense, i.e., an approximate simultaneous upper triangularization that reveals the "average eigenstructure" should be calculated.

Hence, in least square sense, we want to minimize some cost function with respect to lower triangular part of matrices going to zero. An efficient Jacobi-type technique to achieve such an approximate simultaneous diagonalization is presented in [17] for symmetric matrices and its modified version for nonsymmetric matrices is proposed in [18]. The details are in [17] and [18] and need not be repeated here. The cost function is given as:

$$\mathcal{C}(\mathcal{O}) = ||\mathcal{L}(\mathcal{O}^T\ \Upsilon_\psi\ \mathcal{O})||_F^2 + ||\mathcal{L}(\mathcal{O}^T\ \Upsilon_\theta\ \mathcal{O})||_F^2 + ||\mathcal{L}(\mathcal{O}^T\ \Upsilon_\phi\ \mathcal{O})||_F^2$$

over the set of orthogonal matrices $\mathcal{O} \in \mathbb{R}^{p\times P}$ that can be written as products of elementary Jacobi rotations. $||\cdot||_F$ denotes the Frobenius-norm. $\mathcal{L}(\cdot)$ is defined as an operation that extracts the

strictly lower triangular part and the elements on the main diagonal to zero.

In Jacobi-type algorithms, the orthogonal matrix $\mathcal{O}$ is decomposed into a product of elementary Jacobi rotations

$$\mathcal{O}_{qp} = \begin{bmatrix} 1 & \cdots & 0 & \cdots & 0 & \cdots & 0 \\ \vdots & \ddots & \vdots & & \vdots & & \vdots \\ 0 & \cdots & c & \cdots & s & \cdots & 0 \\ \vdots & & \vdots & \ddots & \vdots & & \vdots \\ 0 & \cdots & -s & \cdots & c & \cdots & 0 \\ \vdots & & \vdots & & \vdots & \ddots & \vdots \\ 0 & \cdots & 0 & \cdots & 0 & \cdots & 1 \end{bmatrix}$$

such that

$$\mathcal{O} = \prod_{\#\text{ of sweeps}} \prod_{q=1}^{P} \prod_{p=1}^{q-1} \mathcal{O}_{qp}$$

Here, Jacobi rotations $\mathcal{O}_{qp}$ are defined as orthogonal matrices where all diagonal elements are one except for the two elements c in rows (and columns) p and q. Likewise, all off-diagonal elements of $\mathcal{O}_{qp}$ are zero except for the two elements s and $-s$. The real numbers $c = \cos\vartheta$ and $s = \sin\vartheta$ are the cosine and sine of a rotation angle ϑ such that $c^2 + s^2 = 1$. We are developing an iterative procedure to find a particular rotation angle ϑ such that the cost function is minimized, namely the number of sweeps. Then, c and s is obtained and we can have our desired orthogonal matrix $\mathcal{O}$. In this case, Υ_ψ, Υ_θ and Υ_ϕ can be effectively transformed to diagonal matrices simultaneously, thus the challenge of automatic pairing in joint estimation problem is solved.

Algorithm 1: Three-Dimensional Unitary ESPRIT Outline

Input : Extended data matrix after Hankel constructing and forward-backward averaging
Output: Desired joint estimate of 3D parameters
begin

I. Real processing:

$$\mathbf{HH} = Q_{N_r}\ \mathbf{H}_{\mathrm{FB}}\ Q_{N_N}$$

II. Compute the signal subspace estimate U_s as the P dominant left singular vectors of extended data matrix **HH** (square-root approach)

III. Solve the set of invariance equations by means of LS, TLS or SLS.

$$K_{1\psi}U_s \cdot \Upsilon_\psi = K_{2\psi}U_s$$
$$K_{1\theta}U_s \cdot \Upsilon_\theta = K_{2\theta}U_s$$
$$K_{1\phi}U_s \cdot \Upsilon_\phi = K_{2\phi}U_s$$

IV. Joint frequency estimation by computing the SSD of the real-valued $P \times P$ matrices

$$U_\psi = \mathcal{O}^T\ \Upsilon_\psi\ \mathcal{O}$$
$$U_\theta = \mathcal{O}^T\ \Upsilon_\theta\ \mathcal{O}$$
$$U_\phi = \mathcal{O}^T\ \Upsilon_\phi\ \mathcal{O}$$

V. "Average eigenstructure" should be calculated and the desired 3D parameter joint estimation are obtained

end

Chapter 5

Tensor-based JADE Using ESPRIT

For high order harmonic retrieval problems, since the measurement data is multi-dimensional, current approaches require stacking the dimensions into one highly structured matrix. However, in the conventional subspace estimation step, this stacked data model cannot exploit the essential structure of the original received signal. Thus in this chapter, we introduce tensor, which can be used to store and manipulate high order data in their native multi-dimensional form, to estimate the signal subspace through a high order SVD. This will lead to a better estimate performance because of the improved signal subspace estimate. Furthermore, this new concept and system model can be applied to any multi-dimensional subspace-based parameter estimation scheme. It can be regarded as a whole framework for multi-dimensional harmonic retrieval problems.

5.1 Basic tensor notation and operation

Tensors provide a natural and concise mathematical framework for formulating and solving problems in more and more research areas. They are geometric objects that describe linear relations between scalars, vectors, matrices and other tensors. The order (also degree) of a tensor is the dimensionality of the array needed to represent it, or equivalently, the number of indices needed to label a component of that array. For example, the (i, j, k) element of a third-order tensor $\mathcal{B}$ as $b_{i,j,k}$. An n-mode vector of an $I_1 \times I_2 \times \cdots \times I_N$-dimensional tensor $\mathcal{B}$ is an I_n-dimensional vector

obtained from $\mathcal{B}$ by varying the index i_n and keeping the other indices fixed. Moreover, a matrix unfolding of the tensor $\mathcal{B}$ along the n-th mode is denoted by $[\mathcal{B}]_{(n)}$ and can be understood as a matrix containing all the n-mode vectors of tensor $\mathcal{B}$. We also define the concatenation of two tensors along the n-th mode via the operator $[\mathcal{A} \sqcup_n \mathcal{B}]$. The order of the columns is chosen in accordance with [19], and the following tensor operations we use are also consistent with [19].

- **The outer product** of the tensor $\mathcal{A} \in \mathbb{C}^{I_1 \times I_2 \times \cdots \times I_N}$ and $\mathcal{B} \in \mathbb{C}^{J_1 \times J_2 \times \cdots \times J_M}$ is given by

$$\mathcal{C} = \mathcal{A} \circ \mathcal{B} \in \mathbb{C}^{I_1 \times I_2 \times \cdots \times I_N \times J_1 \times J_2 \times \cdots \times J_M}$$

$$c_{i_1,i_2,\ldots,i_N,j_1,j_2,\ldots,j_M} = a_{i_1,i_2,\ldots,i_N} \cdot b_{j_1,j_2,\ldots,j_M}$$

  In other words, the tensor $\mathcal{C}$ contains all possible combinations of pairwise products between the elements of $\mathcal{A}$ and $\mathcal{B}$. This operator is very closely related to the Kronecker product defined for matrices.

- **The n-mode product** of a tensor $\mathcal{A} \in \mathbb{C}^{I_1 \times I_2 \times \cdots \times I_N}$ and a matrix $U \in \mathbb{C}^{J_n \times I_n}$ along the n-th mode is denoted as

$$\mathcal{B} = \mathcal{A} \times_n U \in \mathbb{C}^{I_1 \times I_2 \times \cdots \times I_{n-1} \times J_n \times I_{n+1} \times \cdots \times I_N}$$

$$b_{i_1,i_2,\ldots,i_{n-1},j_n,i_{n+1},\ldots,i_N} = \sum_{i_n=1}^{I_n} a_{i_1,i_2,\ldots,i_N} \cdot u_{j_n,i_n}.$$

  It may be visualized by multiplying all n-mode vectors of $\mathcal{A}$ from the left-hand side by the matrix U.

- **The higher-order SVD (HOSVD)** of a tensor $\mathcal{A} \in \mathbb{C}^{I_1 \times I_2 \times \cdots \times I_N}$ is given by

$$\mathcal{A} = \mathcal{S} \times_1 U_1 \times_2 U_2 \cdots \times_N U_N$$

  where $\mathcal{S} \in \mathbb{C}^{I_1 \times I_2 \times \cdots \times I_N}$ is the core tensor which satisfies the all-orthogonality conditions and $U_n \in \mathbb{C}^{I_n \times I_n}, n = 1, 2, \ldots, N$ are the unitary matrices of n-mode singular vectors.

5.2 Tensor-based Joint Estimation Using Standard ESPRIT

Starting from **H**, the multi-dimensional channel data after Hankel constructing , we need to represent it in its tensor form rather than stacking it into a highly structured matrix. The original measurement samples are given by:

$$h_{m_1,m_2,m_3,m_4} = \sum_{\ell=1}^{P} \alpha_\ell e^{-j(m_1-1)u_\ell} \cdot e^{-j(m_2-1)v_\ell} \cdot e^{-j(m_3-1)\varpi_\ell} \cdot e^{-j(m_4-1)\varpi_\ell} + d_{m_1,m_2,m_3,m_4}$$

where $m_1 = 1,2,\ldots,M_1, m_2 = 1,2,\ldots,M_2, m_3 = 1,2,\ldots,M_3$ and $m_4 = 1,2,\ldots,LV-1$. For notation simplicity, we denote $N = LV-1$ because $LV-1$ is the number of time domain samples of the known pulse shape function. d_{m_1,m_2,m_3,m_4} represents the zero mean additive noise component inherent in the measurement process.

In order to arrive at a more compressed formulation of the data model, we collect all the samples h_{m_1,m_2,m_3,m_4} into one multi-dimensional array (MDA). Specifically, let $x_\ell = \alpha_\ell$, the 4-dimensional channel estimates $\mathcal{H}$ can be expressed as:

$$\mathcal{H} = \mathcal{A} \times_4 X^T + \mathcal{D}. \tag{5.1}$$

Here, X is the $P \times N$ vectorized matrix of attenuated amplitude. $\mathcal{H} \in \mathcal{C}^{M_1 \times M_2 \times M_3 \times N}$ denotes all estimated impulse response samples, while $\mathcal{D} \in \mathcal{C}^{M_1 \times M_2 \times M_3 \times N}$ collects all the estimation noise samples. $\mathcal{A} \in \mathcal{C}^{M_1 \times M_2 \times M_3 \times P}$ is referred to as the *array steering tensor*, which can be expressed as $\mathcal{A} = \mathcal{I}_{4,P} \times_1 A^{(1)} \times_2 A^{(2)} \times_3 A^{(3)}$, $\mathcal{I}_{4,P}$ is the defined rank-4 identity tensor with each mode a $P \times P$ identity matrix. The array response matrices in each mode are shown to be:

$$A^{(1)} = [a(u_1), a(u_2), \ldots, a(u_P)]$$

$$A^{(2)} = [a(v_1), a(v_2), \ldots, a(v_P)]$$

$$A^{(3)} = [a(\varpi_1), a(\varpi_2), \ldots, a(\varpi_P)]$$

Since we have the identity relationship between matrix and tensor, e.g., $A = [\mathcal{A}]^{T}_{(R+1)}$, which means the matrix is equal to the transpose of the unfolding of the measurement tensor along the last dimension. The tensor-based data model can be equivalently transformed to the matrix-based data model in frequency domain. Most approaches and results obtained from matrix point of view are ready to apply for the tensor case.

For now, We apply FBA and the following real-valued subspace estimation steps are naturally extended to the tensor case. Concepts and principles of FBA have already been introduced in chapter 4, thus we just write out the tensor version of FBA:

$$\mathcal{H}_{\text{fba}} = [\mathcal{H} \sqcup_4 (\mathcal{H}^* \times_1 \Pi_{M_1} \times_2 \Pi_{M_2} \times_3 \Pi_{M_3} \times_4 \Pi_N)]$$

Note that, the FBA tensor $\mathcal{H}_{\text{fba}}$ for each measurement tensor is centro-Hermitian, which possess a bunch of good properties for analytical assessment. The centro-Hermitian tensor is the extension of centro-Hermitian matrix, which can be transformed into real-valued tensor by n-mode product with unitary matrices. It is at this point that unitary ESPRIT comes into picture.

Similarly, recall section 3.2, we need to construct three unitary matrices Q_{M_1}, Q_{M_2} and Q_{M_3} corresponding to the delay, elevation and azimuth array steering vector. Assuming $M_1 = 2Q_1, M_2 = 2Q_2$ and $M_3 = 2Q_3$ which are all even numbers, we have

$$Q_{M_1} = \frac{1}{\sqrt{2}} \begin{bmatrix} I_{Q_1} & jI_{Q_1} \\ \Pi_{Q_1} & j\Pi_{Q_1} \end{bmatrix} \quad Q_{M_2} = \frac{1}{\sqrt{2}} \begin{bmatrix} I_{Q_2} & jI_{Q_2} \\ \Pi_{Q_2} & j\Pi_{Q_2} \end{bmatrix} \quad Q_{M_3} = \frac{1}{\sqrt{2}} \begin{bmatrix} I_{Q_3} & jI_{Q_3} \\ \Pi_{Q_3} & j\Pi_{Q_3} \end{bmatrix}.$$

Furthermore, we define the left Π-real unitary matrices of odd order as:

$$Q_{M_1'} = \frac{1}{\sqrt{2}} \begin{bmatrix} I_{Q_1'} & \mathbf{0}_{Q_1' \times 1} & jI_{Q_1'} \\ \mathbf{0}_{1 \times Q_1'} & \sqrt{2} & \mathbf{0}_{1 \times Q_1'} \\ \Pi_{Q_1'} & \mathbf{0}_{Q_1' \times 1} & j\Pi_{Q_1'} \end{bmatrix} \quad Q_{M_2'} = \frac{1}{\sqrt{2}} \begin{bmatrix} I_{Q_2'} & \mathbf{0}_{Q_2' \times 1} & jI_{Q_2'} \\ \mathbf{0}_{1 \times Q_2'} & \sqrt{2} & \mathbf{0}_{1 \times Q_2'} \\ \Pi_{Q_2'} & \mathbf{0}_{Q_2' \times 1} & j\Pi_{Q_2'} \end{bmatrix}$$

$$Q_{M_3'} = \frac{1}{\sqrt{2}} \begin{bmatrix} I_{Q_3'} & \mathbf{0}_{Q_3' \times 1} & jI_{Q_3'} \\ \mathbf{0}_{1 \times Q_3'} & \sqrt{2} & \mathbf{0}_{1 \times Q_3'} \\ \Pi_{Q_3'} & \mathbf{0}_{Q_3' \times 1} & j\Pi_{Q_3'} \end{bmatrix},$$

where $Q_1^{'} = (M_1 - 1)/2$, $Q_2^{'} = (M_2 - 1)/2$ and $Q_3^{'} = (M_3 - 1)/2$.

Before utilizing any subspace-based parameter estimation scheme, we need to estimate a basis for the multi-dimensional signal subspace from the noisy observations. Similarly, the tensor-based signal subspace estimation can be achieved through a truncated higher-order singular value decomposition (HOSVD) of $\mathcal{H}_{\text{fba}}$ [16]:

$$\mathcal{H}_{\text{fba}} \approx \hat{\mathcal{S}} \times_1 \hat{U}_1 \times_2 \hat{U}_2 \times_3 \hat{U}_3 \times_4 \hat{U}_4 \tag{5.2}$$

where $\hat{\mathcal{S}} \in \mathcal{C}^{p_1 \times p_2 \times p_3 \times N}$ is the truncated core tensor and $\hat{U}_r \in \mathcal{C}^{M_r \times p_r}$ for $r = 1, 2, 3$, $\hat{U}_4 \in \mathcal{C}^{P \times N}$ are the matrices of dominant r-mode singular vectors. p_r represents the rank of r-mode singular matrix unfolding. Actually, the HOSVD is computed through SVDs of the unfoldings. Based on (5.2), a tensor-based subspace estimate can be written as:

$$\mathcal{U}^{[s]} \approx \hat{\mathcal{S}} \times_1 \hat{U}_1^{[s]} \times_2 \hat{U}_2^{[s]} \times_3 \hat{U}_3^{[s]} \times_4 \hat{U}_4^{[s]} \tag{5.3}$$

It is already shown in [16] that, an improved signal subspace estimate is achieved using tensor-based HOSVD in the presence of noise and if the number of paths is strictly less than the number of array elements in at least one of the modes. This is because the tensor approach allows us to filter out noise in each of the modes of estimated signal subspace separately which results in an

improved signal subspace. We can see this improvement more clearly through the performance comparison with matrix-based method in subsection 5.3.2.

Assume the 3D array steering tensor features shift-invariance in each of its modes, we can directly apply multi-dimensional standard ESPRIT algorithm to write the shift-invariance equations as:

$$\begin{aligned}
\mathcal{A}_{\times 1} J_{1\ \times 4}^{(1)} \Theta &= \mathcal{A}_{\times 1} J_2^{(1)} \\
\mathcal{A}_{\times 2} J_{1\ \times 4}^{(2)} \Phi &= \mathcal{A}_{\times 2} J_2^{(2)} \\
\mathcal{A}_{\times 3} J_{1\ \times 4}^{(3)} \Psi &= \mathcal{A}_{\times 3} J_2^{(3)}
\end{aligned} \tag{5.4}$$

where Θ, Φ and Ψ are already defined in matrix-based subsection. $J_i^{(r)} \in \mathcal{R}^{(M_r-1)\times M_r}$, $i = 1,2$ represent the selection matrices for the r_{th} mode under maximum overlapping.

$$\begin{aligned}
J_1^{(r)} &= [I_{M_r-1} \ \ \mathbf{0}_{(M_r-1)\times 1}] \\
J_2^{(r)} &= [\mathbf{0}_{(M_r-1)\ \ \times 1} I_{M_r-1}];
\end{aligned}$$

Since the array steering tensor approximately span the same vector space as the estimated signal subspace $\mathcal{U}^{[s]}$ similar to the matrix case:

$$\mathcal{A} \approx \mathcal{U}_{\times 4}^{[s]} \bar{T}$$

for some $P \times P$ nonsingular transform matrix $\bar{T}$. We may substitute the above relation back to (5.4):

$$\begin{aligned}
\mathcal{U}_{\times 1}^{[s]} J_{1\ \times 4}^{(1)} \Theta &\approx \mathcal{U}_{\times 1}^{[s]} J_2^{(1)} \\
\mathcal{U}_{\times 2}^{[s]} J_{1\ \times 4}^{(2)} \Phi &\approx \mathcal{U}_{\times 2}^{[s]} J_2^{(2)} \\
\mathcal{U}_{\times 3}^{[s]} J_{1\ \times 4}^{(3)} \Psi &\approx \mathcal{U}_{\times 3}^{[s]} J_2^{(3)}
\end{aligned}$$

In case of unitary ESPRIT, the selection matrices need to be updated a little bit using the unitary

matrices we have defined above.

$$\begin{aligned} K_{1\psi}\mathcal{U}^{[s]} \cdot \Upsilon_{\psi} &= K_{2\psi}\mathcal{U}^{[s]} \\ K_{1\theta}\mathcal{U}^{[s]} \cdot \Upsilon_{\theta} &= K_{2\theta}\mathcal{U}^{[s]} \\ K_{1\phi}\mathcal{U}^{[s]} \cdot \Upsilon_{\phi} &= K_{2\phi}\mathcal{U}^{[s]} \end{aligned} \tag{5.5}$$

where the three corresponding pairs of transformed selection matrices are given by:

$$\begin{aligned} K_{1\psi} &= 2 \cdot \mathrm{Re}\{Q_{M_1'}^H J_2^{(1)} Q_{M_1}\} \quad & K_{2\psi} &= 2 \cdot \mathrm{Im}\{Q_{M_1'}^H J_2^{(1)} Q_{M_1}\} \\ K_{1\theta} &= 2 \cdot \mathrm{Re}\{Q_{M_2'}^H J_2^{(2)} Q_{M_2}\} \quad & K_{2\theta} &= 2 \cdot \mathrm{Im}\{Q_{M_2'}^H J_2^{(2)} Q_{M_2}\} \\ K_{1\phi} &= 2 \cdot \mathrm{Re}\{Q_{M_3'}^H J_2^{(3)} Q_{M_3}\} \quad & K_{2\phi} &= 2 \cdot \mathrm{Im}\{Q_{M_3'}^H J_2^{(3)} Q_{M_3}\} \end{aligned}$$

As before, equation (5.5) represents a tensor least squares problem, and the solution is given by:

$$\begin{aligned} \Upsilon_{\psi}^T &= \left(\hat{K_{1\psi}} \cdot \left[\mathcal{U}^{[s]}\right]_4^T\right)^{\dagger} \cdot \hat{K_{2\psi}} \cdot \left[\mathcal{U}^{[s]}\right]_4^T \\ \Upsilon_{\theta}^T &= \left(\hat{K_{1\theta}} \cdot \left[\mathcal{U}^{[s]}\right]_4^T\right)^{\dagger} \cdot \hat{K_{2\theta}} \cdot \left[\mathcal{U}^{[s]}\right]_4^T \\ \Upsilon_{\phi}^T &= \left(\hat{K_{1\phi}} \cdot \left[\mathcal{U}^{[s]}\right]_4^T\right)^{\dagger} \cdot \hat{K_{2\phi}} \cdot \left[\mathcal{U}^{[s]}\right]_4^T \end{aligned}$$

where

$$\begin{aligned} \hat{K_{1\psi}} &= K_{1\psi} \otimes I_{M_1M_2} \quad & \hat{K_{2\psi}} &= K_{2\psi} \otimes I_{M_1M_2} \\ \hat{K_{1\theta}} &= I_{M_3M_2} \otimes K_{1\theta} \quad & \hat{K_{2\theta}} &= I_{M_3M_2} \otimes K_{2\theta} \\ \hat{K_{1\phi}} &= I_{M_3M_1} \otimes K_{1\phi} \quad & \hat{K_{2\phi}} &= I_{M_3M_1} \otimes K_{2\phi} \end{aligned}$$

The HOSVD-based subspace estimate $\left[\mathcal{U}^{[s]}\right]_4^T$ defined in (5.3) is linked to the SVD-based subspace estimate $\hat{U}_s$ via the following algebraic relation:

$$\left[\mathcal{U}^{[s]}\right]_4^T = (\hat{T}_1 \otimes \hat{T}_2 \otimes \hat{T}_3) \cdot \hat{U}_s$$

where $\hat{T}_r \in \mathbb{C}^{M_r \times M_r}$ represent estimates of the projection matrices onto the r-modes of measurement tensor, which are computed via $\hat{T}_r = \hat{U_r^{[s]}} \hat{U_r^{[s]}}^H$.

The final step of the 3-D unitary ESPRIT algorithm is still the SSD operation, to make different modes of measurement tensor share the same set of eigenvectors. This guarantees the correct pairing of the paths over modes. The idea is exactly the same with matrix-based ESPRIT algorithm, so it is unnecessary to write out again.

5.3 Matrix and Tensor-based Unitary ESPRIT Algorithm Simulation

In this section, we evaluate both matrix-based and tensor-based joint estimation algorithm under various antenna configurations, to see the impact of practical implementation on estimation performance. Assume it is a two paths situation with DoAs $[70, 77]^\circ$ for elevation and $[45, 60]^\circ$ for azimuth, path fading amplitudes $[1, 0.8]$ and time delay $[0.5, 2.1]s$, same as 2D joint angle estimation scenario. Additionally, we set the stacking number of Hankel construction to be 2. The number of sweeps in SSD operation is determined as 10. All the results are based on 1000 Monte-Carlo runs under SNR ranging form 6 dB to 24 dB. Here, the definition of SNR is the signal to noise ratio for the channel, which is impacted by the multi-paths effect. Originally, the signal power is always assumed to be 1 after normalization, but for our two paths scenario (one main path, one off-main path), the signal power should be the sum of these two paths' signal power. We will first compare the estimation performance between separate 2D joint angle and delay estimation with matrix-based 3D JADE. Then the comparison between matrix and tensor-based 3D JADE follow up.

5.3.1 Comparison between 2D Joint Angle Estimation and Matrix-based 3D JADE Estimation

For delay estimation, we can see that different antenna configurations don't have much impact on the estimation performance, as shown in Fig. 5.1(a) and Fig. 5.1(b). We found that this result is not surprising since we can see it from the Fisher Information Matrix derived in [12]. The performance depends on the total number of antenna elements (e.g., in our case, $N_r = M_1 M_2 M_3$) rather than the various configurations. Note that, once the total number of antenna elements is fixed, the estimation accuracy of delay only depends on the DFT matrix given in (2.7).

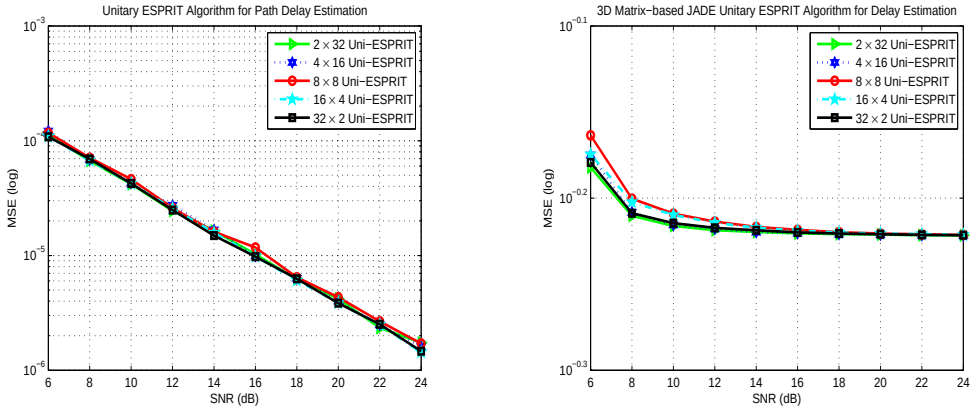

(a) (b)

Figure 5.1: Comparison Between 2D Separate and 3D Matrix-based Joint Delay Estimation

Fig. 5.2(a) and Fig. 5.2(b) shows that, for elevation angle estimation, its performance is proportional to the number of antennas vertically. This matches with our conventional understanding because for 1D antenna array, a larger number of antenna elements will contribute to a better performance intuitively. Moreover, we may compare the trend of Fig. 5.2(b) with Fig. 5.2(a) to obtain that, the elevation angle estimation is actually impacted by the delay estimation through this joint algorithm. In low SNR regime, even a 32×2 antenna configuration doesn't contribute much to the elevation estimation performance, only when we operate in high SNR regime, the advantage of more antennas will exhibit. Another point is that, as CRLB suggests, the more parameters we are trying to estimate, the more uncertainty will be involved. Hence, for any of these configura-

tions, the MSEs of 3D JADE joint elevation estimation is much higher than those of 2D joint angle estimation, e.g., more than a magnitude of order.

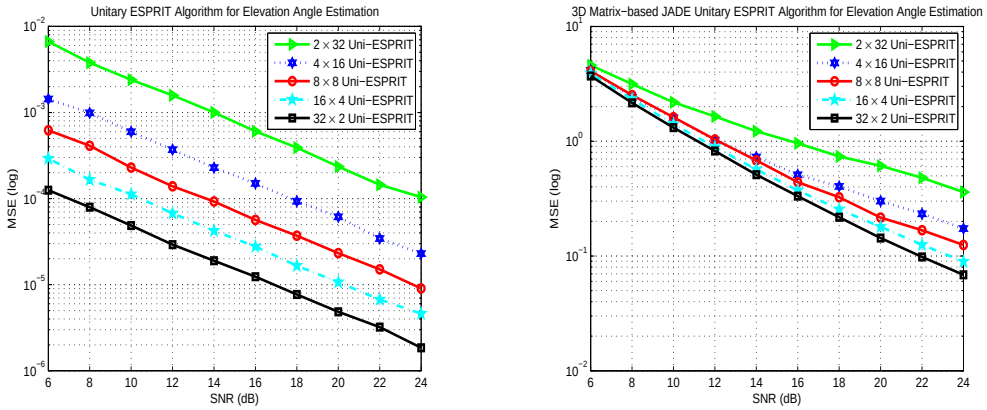

(a) (b)

Figure 5.2: Comparison Between 2D Joint and 3D Matrix-based Joint Elevation Angle Estimation

Another interesting finding of joint azimuth angle estimation is illustrated in Fig. 5.3(a) and Fig. 5.3(b). We can see that a 4×16 configuration gives out a better performance than 2×32. The result is similar to our former observation in [12] and has been analyzed analytically in [20]. This means, for joint estimation of three parameters, we can still get the fact that, azimuth angle estimation is indeed affected by the estimation performance of elevation angle. In the case of the 2×32 array, the performance of elevation estimation is so poor that it affects the performance of azimuth estimation. We can also observe that in the low SNR regime, all curves merges together. This is because when SNR is too low, we can't get accurate estimate for θ, ϕ and τ, no matter for what kind of antenna configurations. As the SNR increases, the impact of antenna configuration comes into the picture as shown in Fig. 5.3(b).

Though 3D joint estimation scheme give out much worse estimation performance than separate estimation, we need to make sure that they are automatically correct-pairing. As 3D algorithm exhibits, joint estimation will give out a better resolution than the separate ones. This is due to the fact that the ESPRIT-like algorithm takes advantage of all the information of received signals from all the antenna elements. And now, we can resolve a larger number of rays in cases where two or more rays have equal DoAs or delays.

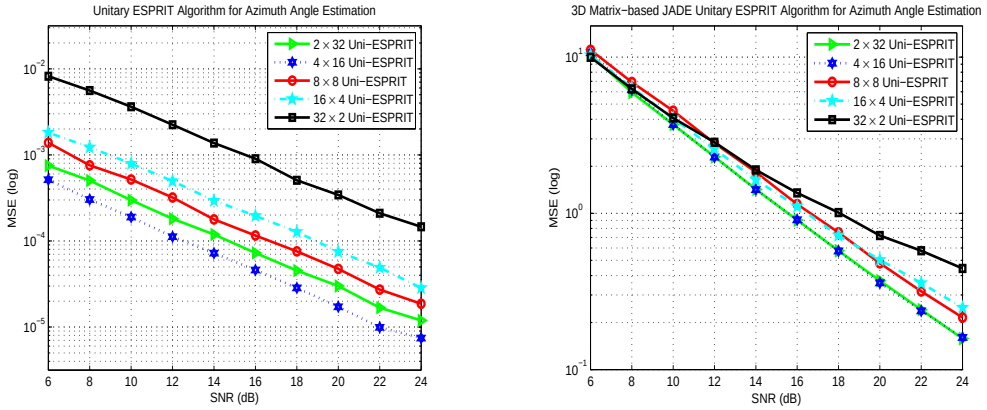

(a) (b)

Figure 5.3: Comparison Between 2D Joint and 3D Matrix-based Joint Azimuth Angle Estimation

5.3.2 Comparison between 3D Matrix and Tensor-based JADE Algorithm

For delay estimation, we can still see that different antenna configurations don't have much impact on the estimation performance, as shown in Fig. 5.4(a) and Fig. 5.4(b). However, tensor-based approach outperforms matrix-based method, especially when operating in low SNR regime because of its noise-filtering property.

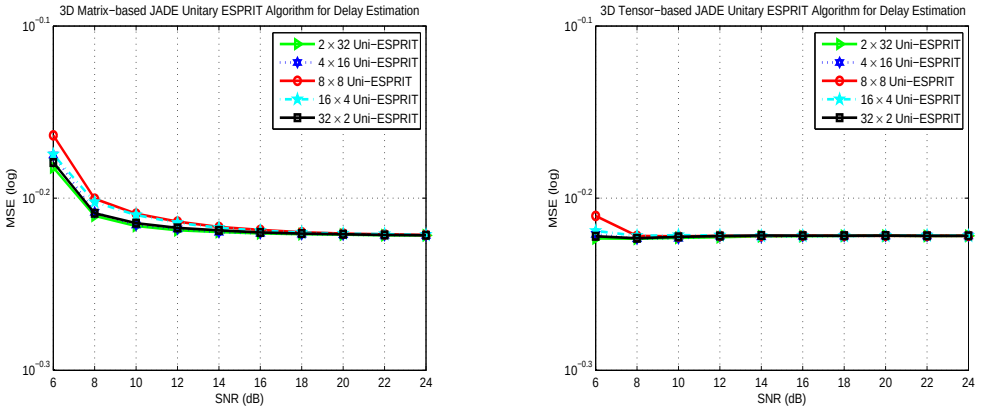

(a) (b)

Figure 5.4: Comparison Between 3D Matrix and Tensor-based Joint Delay Estimation

Fig. 5.5 and Fig. 5.6 shows similar trend of MSE between matrix and tensor-based approach, the main differences are:

- The joint estimation performance of tensor is obviously better than that of matrix.

- Fig. 5.5(b) and Fig. 5.6(b) look more separate. But in Fig. 5.5(a) and Fig. 5.6(a), especially in low SNR regime, curves are overlapping because they are effected by each other if using matrix-based joint estimation scheme.

- For tensor-based elevation angle estimation in low SNR regime, a 16×4 configuration is better than that of 32×2 configuration, which is different from matrix-based results.

As we know, tensor restores the multi-dimensional data in its natural structure, which can be regarded as separate processing. It allows us to filter out noise in each of the modes of estimated signal subspace separately which results in an improved signal subspace. Another point is, we always focus on azimuth angle estimation is because, for a fixed number of total antenna elements, the azimuth angle estimation is more crucial for MIMO beam-forming in cellular systems. For tensor-based approach, we observe again the fact that a 4×16 configuration is better than that of 2×32 configuration. Combined with our simulation and analytical results, we may say that a more symmetrical structure leads to a relatively smaller MSE.

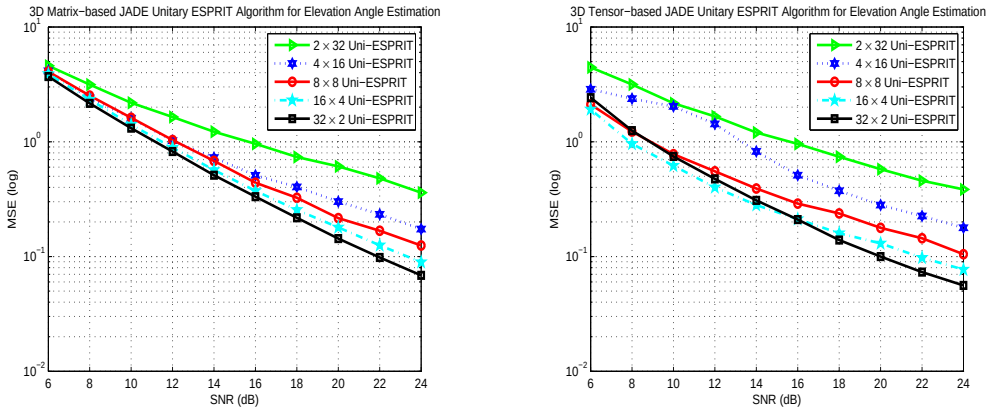

(a) (b)

Figure 5.5: Comparison Between 3D Matrix and Tensor-based Joint Elevation Angle Estimation

Therefore, the tensor-based approach gives out a even better performance as compared in Fig. 5.4, Fig. 5.5 and Fig. 5.6. We can see that almost a half magnitude of order improvement is obtained for all three parameter estimation.

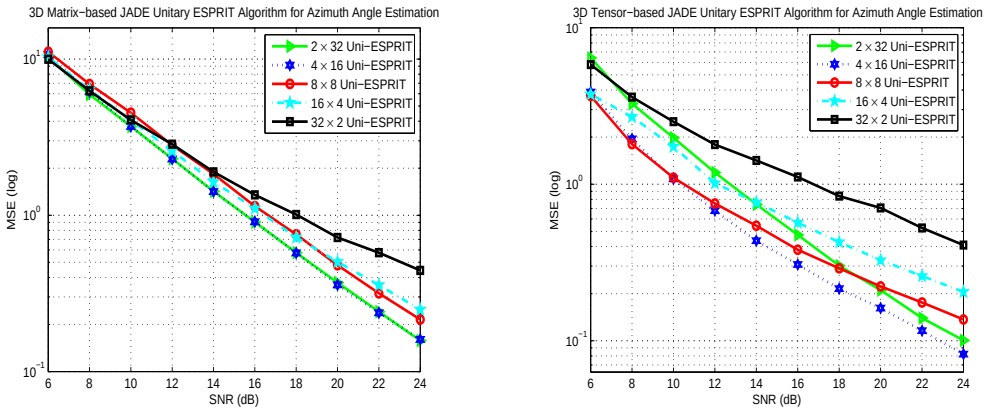

(a) (b)

Figure 5.6: Comparison Between 3D Matrix and Tensor-based Joint Azimuth Angle Estimation

Chapter 6

Conclusion and Future Work

The thesis illustrates the application of DoA estimation technique (ESPRIT algorithm) to a 2D Massive MIMO broadband communication regime and jointly estimate the 3D channel parameters: elevation angle, azimuth angle and path delay, which is crucial for downlink digital beamforming in cellular networks. The fundamental assumption is that antenna array at the base station should possess some particular structures, e.g., if it can be divided into two same sub-arrays.

ESPRIT algorithm uses the relationship between eigenspace of two divided array output matrices to obtain our desired parameters, and the complexity is very promising compared to MUSIC and MLE. Since multi-dimensional MUSIC and MLE approach both need a search along the whole multi-dimensional space, while ESPRIT works well without the exhaustive search. The linearity property between signal subspace and array manifold, and the invariance property between two sub-arrays highlight the advantage of ESPRIT, since multi-dimensional extension, real processing, joint diagonalization, forward-backward averaging etc. are easily incorporated compared to other DoA estimation approaches.

We observe that azimuth angle estimation actually couples with elevation angle estimation. In circumstances where elevation angle estimation performance is so poor, it affects our azimuth performance. Furthermore, different antenna configurations will contribute to different estimation performance, as well as capacity loss. In general, a more symmetrical antenna configuration leads

to a relatively better estimation performance as for the design of antenna arrays at the base station. The last thing to note is that various antenna configurations don't have much impact to path delay estimation as long as the total number of antenna array elements is fixed. It only depends on the DFT matrix, or simply the number of snapshots when you sample the known pulse shape function.

Improved results could be obtained by the application of tensor processing. Tensor is a powerful geometric tool and widely used in signal processing and wireless communication area [10]. It helps us store, retrieve, process the measurement data in its original form, and separate mode processing can effectively filter out the noise compared to matrix-based methods. More importantly, tensor processing will give us a better signal subspace estimate, which is beneficial for all subspace-based estimation algorithms. It is a whole new framework rather than just a simple preprocessing step.

There are still many aspects we can investigate in the future, e.g., large scale MIMO, multi-user scenario, other DoA estimation techniques with multi-dimensional extension, how training will affect the estimation performance within OFDM, correct pairing between different sub-carriers if one user can be supplied with more than one sub-carrier and analytical assessment in multi-path, multi-user case, etc.

- When large scale MIMO is involved, many results obtained before are no longer valid because random matrix theory kicks in. Only asymptotic behaviour is shown by now [21, 22], but no practical implementation is there. Samsung is developing a Full Dimension MIMO (FD-MIMO) [6] technology in the context of next generation evolution towards B4G and 5G cellular systems, which relies on the 2D base station antenna array. Even they analyze the system performance asymptotically, the prototype is still quite small comparing to the MIMO definition, a 32×64 2D antenna array.

- Giuseppe Caire propose Joint Spatial Division and Multiplexing (JSDM) in [23] , an approach to multi-user MIMO downlink that exploits the structure of the correlation of the channel vectors in order to allow for a large number of antennas at the base station while requiring reduced-dimensional Channel State Information at the Transmitter (CSIT). Two

dimensional base station antenna array, DFT-based pre-beamforming, random matrix theory, fairness criteria are all involved.

- In [24], A. Lee and Thomas compares the most popular DoA estimation techniques with their multi-dimensional extensions in great detail, and showed us that MD-MLE outperforms all algorithms with respect to MSE, except for its high computational cost. And one-dimensional MUSIC outperforms all of the MD algorithms for random angle-independent array perturbations. Hence for different applications, we may consider MUSIC or MLE instead of ESPRIT from time to time.

- In our paper, we assume that the channel frequency response estimate is available. However, in practical situation, it is quite hard to get the estimate even we use the training sequence. Furthermore, how much training is proper is another interesting topic to look at [25]. Pilot contamination is also severe and has great impact to channel estimation performance when we are in multi-cell system [26].

- Closed-form results can give us more intuition and theoretically confirm the simulated observations we had made. In [27], Haardt et al. already show the derivation of closed-form MSE expressions using tensor-based multi-dimensional Unitary ESPRIT algorithm, in single source case. Equivalently in our situation, only the single path problem is analytically assessed. Multi-path and multi-user results are surely helpful if derived as benchmark.

Therefore, this paper lays a good foundation for further analysis and test on future design of practical broadband MIMO-OFDM wireless communication system.

Part II

Analysis of Direction of Arrival Estimation Algorithms for Basal Ice Sheet Tomography

Chapter 7

Introduction

Scientific research indicates the current sea level rise is about 3.5 mm per year worldwide. According to the US National Oceanic and Atmospheric Administration (NOAA) [28], this is a significantly larger rate than the sea level rise averaged over the last several thousand years, and the rate may be increasing. This trend puts thousands of coastal cities, islands and natural environments at risk in the future. The rise in sea level is contributed through two major factors: one is thermal expansion, the other is the melting of glaciers and polar ice sheets. The latter of which is the primary interest of this work. Analysis of the geological record suggests there is ice loss in Greenland and West Antarctica due to global warming. To have knowledge of the current ice mass balance and to predict ice sheet dynamics in these two regions, we need to know the ice sheet thickness and the physical properties of the ice sheet surface and bed. In this regard, we require the estimation of basal ice sheet topography at fine resolution and over extensive portions of the polar ice sheets.

There are several methods that can be used to observe the basal conditions of an ice sheet as discussed in [29]. The most direct way is drilling a borehole to the bottom of the ice sheet and passing the measurement equipment down into the borehole. However, wide area coverage with fine resolution is infeasible. Similarly, seismic studies are popular over the decades and can fulfill many of the scientific requirements, but can't achieve the wide area coverage. Radar-based

sounding tomography is the only method that can achieve wide area coverage through remote sensing, with advantages including lower operational costs, finer spatial and temporal resolution, higher measurement accuracy, etc. Here, we aim to obtain an accurate estimate of basal roughness and bed conditions from the backscattered signal collected over a large swath.

In this thesis, the datasets considered for bed topography measurements were taken using the Multi-channel Coherent Radar Depth Sounder (MCoRDS) which also enables 3D imaging and observations of deep internal layering [30]. This wideband SAR includes a receive antenna array with multiple phase centers, to resolve ambiguities in the cross-track dimension using array processing techniques (e.g., DoA estimation algorithms). In order to maximize the coverage rate, the radar should image on both sides of the platform. The geometry of our synthetic aperture radar is shown in Fig.7.1. Taking the SAR image formed from each receive antenna array element, we

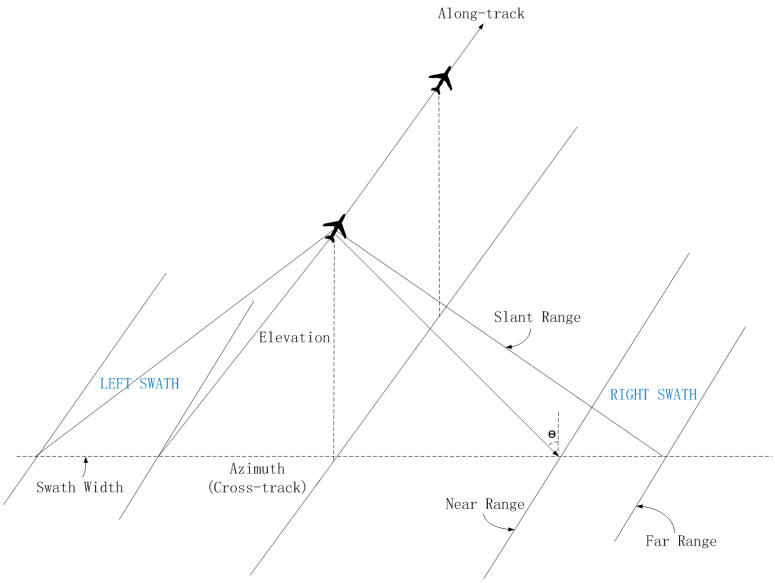

Figure 7.1: Synthetic Aperture Radar System Geometry for Left and Right Swaths

apply tomographic techniques to generate fine-resolution bed topography from single-pass data (the system model is detailed in section 8.2). Since the ultimate goal of this work is to estimate the ice bottom elevation, we use cross-over analysis from multiple crossing flightlines to verify the self-consistency of the tomographic algorithms since the elevation is not a function of the location or orientation of the data collection.

In [31, 32], Paden et al. applied parametric signal processing algorithms to derive fine-resolution three-dimensional (3D) images of the ice bottom. Due to the computational complexity of the optimal MLE approach, Paden suggests using the subspace-based method, MUSIC, to solve the problem. By comparing parallel and perpendicular tracks and showing the difference is small, the results have been shown to be self-consistent. Raghunandan introduced an alternating projection based ML approach to reduce its computational burden [30], and describes applications of MUSIC, MLE and RISR (ReIterative SuperResolution algorithm) to the problem at hand in detail.

In this work we apply and analyze two different types of DoA estimation techniques, MUSIC and MLE-AP. For the antenna array geometry and sample support used in our tomographic application, the surface extraction routine of MUSIC performs better originally in terms of cross-over analysis. However, after several improvements applied to MLE, i.e., replacing ideal steering vector generation with measured steering vectors, automatic determination of the number of scatter sources, smoothing the 3D tomography in order to get a more accurate height estimation and introducing a quality metric for the estimated signals, etc., the surface extraction routine of MLE outperforms MUSIC. Additionally, a simple two pass multi-resolution grid search technique is applied to significantly reduce the processing time of MLE.

The rest of the thesis is organized as follows. In Chapter 8, the system model and problem formulation is described. Two different methods for DoA estimation, MUSIC and MLE-AP are introduced. In Chapter 9, several improvements to the surface extraction routine of the MLE approach are illustrated and applied. The SAR focused datasets provide a good case study to explore the performance of MUSIC and MLE to the application of ice bed elevation estimation. The strong self-consistency of cross-over plots confirms that the modified surface tracking routine of MLE indeed works well for our particular ice bed tomographic application. Finally, in Chapter 10 we provide a summary and our conclusions as well as list topics for future work.

Chapter 8

Modeling and Approaches

8.1 Overview

As introduced in chapter 7, improved ice bottom height estimation is possible if proper post-processing of migrated SAR images can be done. Since the problem is essentially a DoA estimation problem, which has been researched for decades with a wide range of applications, we can apply some well-known algorithms to our dataset and obtain more accurate ice bed measurements. Note that, both this problem and the JADE formulation in Part I belong to the same type: the localization of radiating sources by sensor arrays. Only the scenario and some of the underlying assumptions are different. In practice, localization is made difficult by the fact that there are usually an unknown number of signals impinging on the array simultaneously, each from unknown directions and with unknown amplitudes. Also, the received signals are always corrupted by noise. Additionally, array calibration errors, various signal-to-noise ratio (SNR) levels, signal and noise model mismatch, space-time correlation, available sample support, array geometry, propagation media, interference and many more aspects contribute to the final estimation performance.

Since there is a Fourier relationship between the beam pattern and the excitation at the array, this allows the DoA estimation problem to be treated as equivalent to spectral estimation. As for spectral analysis, we have non-parametric methods (e.g., peridogram, correlogram, Capon)

and parametric methods (e.g., ARMA based, model-fitting based and signal subspace based approaches). The need for fine-resolution in array signal processing requires parametric approaches, especially the subspace-based approaches. These subspace-based methods are well-suited for most DoA estimation problems because they work best when the number of sources is small compared to the number of measurements, and normally, this is the case.

A variety of techniques for conquering this type of problems have been proposed. The maximum likelihood estimator (MLE) technique was one of the first to be investigated, and is generally regarded as optimal with respect to MSE. Its performance is generally satisfying, and it can handle low SNR, the coherent signal case and the low sample support situation. Nonetheless, because of the high computational load of the multivariate nonlinear maximization problem involved, it wasn't widely used. Instead, suboptimal techniques with reduced computational load have dominated the field, the best known one is MUSIC (MUltiple SIgnal Classfication) [33]. Combined with incoherent/coherent averaging, forward-backward averaging, spatial smoothing and the extension root-MUSIC algorithm, it can achieve almost the same estimation performance or even better than MLE with much less complexity. Recently, the MUSIC algorithm serves as the benchmark for many DoA estimation problems.

Hence, in our paper, we mainly talk about these two techniques, MUSIC and a fast implementation of MLE, namely MLE-AP. The latter one is based on an iterative technique referred to as "Alternating Projection", that transforms the multivariate nonlinear maximization problem into a sequence of much simpler one-dimensional maximization problems. A detailed algorithm description is given in this chapter and a performance comparison between MUSIC and MLE-AP is discussed in chapter 9.

8.2 System model

The problem set up is shown in Fig. 8.1. The x-axis points in the direction of flight, the y-axis points out the left wing tip during level flight, and the z-axis points upward. As the plane flies over,

the radar pulse scatters off the ice surface, ice bottom, and englacial targets. In this work, we aim to apply DoA estimation algorithms to ultimately estimate the height of the ice bottom to produce a 3D ice bed digital elevation model (DEM).

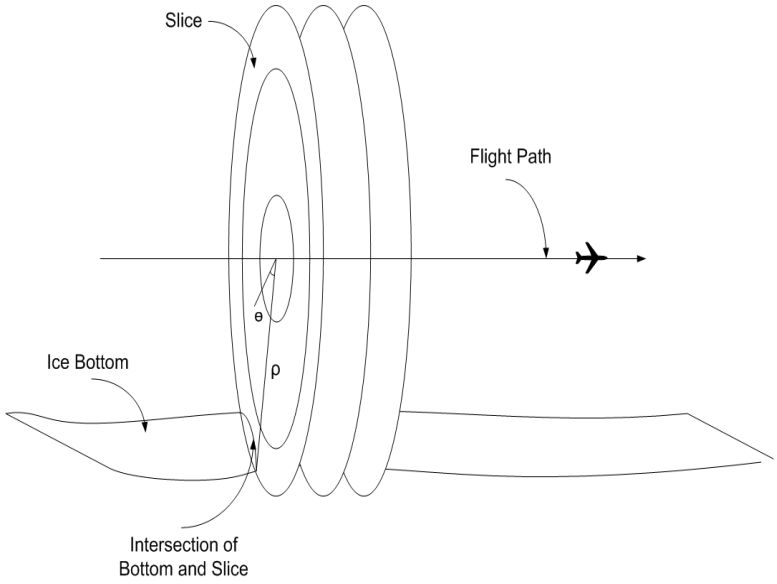

Figure 8.1: Coordinate System for Radar 3D Imaging

To illustrate why our problem at hand is essentially a DoA estimation problem, we break down the 3D topography into thousands of slices in the along-track dimension as shown in Fig.8.1. Targets are resolved to each slice through SAR processing. The radius ρ of each slice is resolved through pulse compression and the resolution is set by the bandwidth of the pulse. At this point we have resolved targets to a thin annulus oriented perpendicular to the flight track. Typically, an echogram contains thousands of resolved annulus rings (range bins in radar terminology). However, since we have a general idea of where the ice bottom is using our regular depth sounding and analysis techniques, we only need to look at a few hundred of these range bins. To resolve where a target is on the annulus we resolve the direction, θ, through DoA estimation techniques. Fig.8.2 shows this problem for a representative ice bottom. If the ice bottom is flat enough, the annulus will intersect it at two points, one on the left and one on the right. This is the ideal situation. If the antenna patterns do not sufficiently suppress the surface clutter, there will be two more ice surface intersections (radar clutter) and there can also be englacial scatters. In many situations though, the

ice surface and englacial scatters are near noise levels and may be ignored.

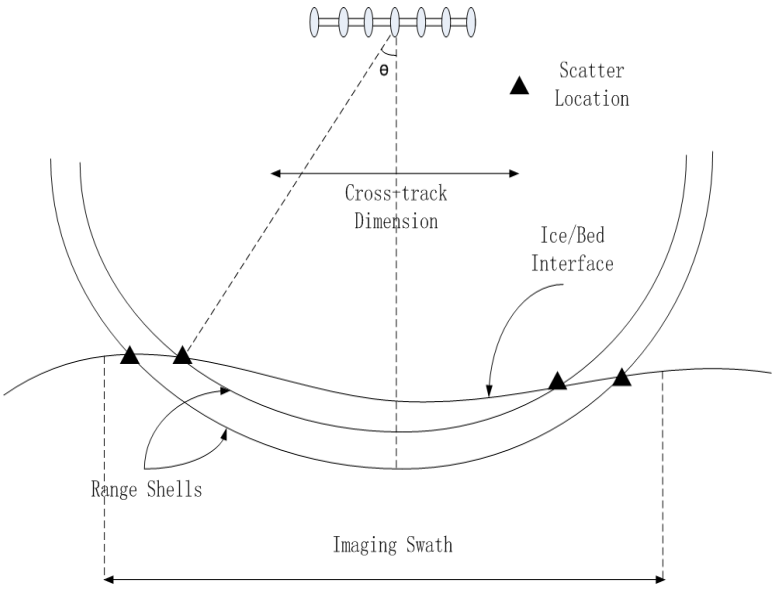

Figure 8.2: Terrain returns and image signatures for a pulse of radar energy

For the purposes of simulation, a simplified version of the array geometry is assumed with zero squint angle. The relationship between the received signals and the sources is given by:

$$X = A(\theta)S + N \tag{8.1}$$

Here, X and N are the received echo signals and zero-mean additive noise samples at a given range bin, respectively (both with dimension $K \times L$). S is the $M \times L$ backscattered signal by the ice/bed interface while $A(\theta)$ denotes the $K \times M$ steering vector matrix. K, L and M represents the number of sensors (i.e., 7 in our airborne-radar system), number of snapshots and number of sources. Breaking matrices out into columns of vectors, (8.1) can be rewritten as:

$$[\mathbf{x}_{t_1}\ \mathbf{x}_{t_2}\ \cdots \mathbf{x}_{t_L}] = [\mathbf{a}(\theta(1))\ \mathbf{a}(\theta(2))\ \cdots \mathbf{a}(\theta(m))] \times [\mathbf{s}_{t_1}\ \mathbf{s}_{t_2}\ \cdots \mathbf{s}_{t_L}] + [\mathbf{n}_{t_1}\ \mathbf{n}_{t_2}\ \cdots \mathbf{n}_{t_L}]$$

where t is the look-index in the along-track dimension, $1 \leq t \leq L$, and m is the source number, $1 \leq m \leq M$.

The final goal is to estimate parameter θ with known array geometry and observation matrix,

X. There are so many approaches to tackle this problem, e.g., the ESPRIT algorithm introduced in Part I of the thesis. However, for our dataset and particular array geometry, we focus on two methods: the subspace-based estimation scheme MUSIC algorithm, and the model-fitting based method Maximum Likelihood estimation. For the sake of simplicity, we will use the result from the MUSIC algorithm as the benchmark and compare it with different improved applications of ML estimators. Ice bottom 3D tomography results will be displayed in section 9.2 of chapter 9.

8.3 MUSIC

MUSIC belongs to a category of subspace based algorithms that is generated from Pisarenko's method [34]. While the main goal is in determining the parameter θ, EigenValue Decomposition (EVD) of the signals' sample correlation matrix, R, helps in analyzing the underlying signal in terms of its eigenvalues and eigenvectors [33]. Owing to the linear independence among these eigenvectors, they can be used as a basis for a vector space, wherein any vector can be expressed as a linear combination of the eigenvectors. In the application to sensor array processing, the vector space comprises signal with noise (U_s) and noise only (U_n) subspaces. The eigenvectors of R, corresponding to the M largest eigenvalues are the signal subspace U_s, while the remaining $K-M$ components constitute the U_n subspace. As we know, these two subspaces are orthogonal to each other. For the purpose of determining DoA only, U_s and U_n can be directly computed from the Singular Value Decomposition (SVD) of the observation matrix X, instead of using EVD of R.

Let the estimated signal and noise subspace denoted by $\hat{U}_s$ and $\hat{U}_n$, respectively, the null spectrum $Q(\theta)$ is then determined by either using $\hat{U}_s$ or $\hat{U}_n$ in the following ways:

$$\text{Signal: } Q(\theta) = \mathbf{a}^H(\theta)[\mathbf{I} - \hat{U}_s\hat{U}_s^H]\mathbf{a}(\theta)$$

or

$$\text{Noise: } Q(\theta) = \mathbf{a}^H(\theta)\hat{U}_n\hat{U}_n^H\mathbf{a}(\theta)$$

where $\mathbf{a}(\theta)$ denotes the steering vector consisting of array response to the DoAs. $\mathbf{I}$ represents the identity matrix. The best choice will depend on the size of M, the number of sources, compared to K, the number of sensors. In most cases, we use $\hat{U}_s$, which corresponds to the largest M eigenvalues, because M is usually less than $M-K$.

Then we plot Q_θ by varying $\mathbf{a}(\theta)$ over $-\pi \leq \theta \leq \pi$ and choose the M minima to determine the values of θ. Note that, in order for MUSIC to work well, a sufficient sample support is required and we have to know the array manifold, also the signals can't be coherent. But the good news is the spectral MUSIC algorithm is applicable to arbitrary array geometries. In the case of correlated sources, averaging over independent snapshots (temporal smoothing) and/or sub-aperture processing within a snapshot (spatial smoothing) may be employed [35].

8.4 Maximum Likelihood Localization by Alternating Projection

As we know, the maximum likelihood estimator is unbiased, with its performance approaching the Cramer-Rao lower bound asymptotically as the sample support goes to infinity [36]. To solve the problem at hand, the following assumptions regarding the array, the signals and the noise are implied [37]:

- The number of sources is known and is smaller than the number of sensors.
- Each set of steering vectors are linearly independent.
- The noise $\{\mathbf{n_t}\}$ is a stationary and ergodic complex-valued Gaussian process of zero-mean, and variance matrix $\sigma^2\mathbf{I}$ with unknown value of variance. The noise samples are statistically independent.

The first two assumptions are needed to make sure there is only one solution. From our ice sheet model in Fig. 8.2, observing model order statistics and our array geometry, we know we can

satisfy the first two assumptions. The noise assumption is conventional in sensor array processing, for analytical simplicity and obtaining closed-form expressions of the MLE. Note that, even when the above assumptions are violated, the estimator to be derived is still meaningful: it coincides with the Least-Squares (LS) estimator.

The maximum likelihood estimates can be broadly categorised as unconditional and conditional maximum likelihood estimates (named UML and CML, respectively). The main difference between them is: UML assumes that the source signals are sample functions of a Gaussian random process, while CML assumes the source signals are unknown but deterministic in nature. Here we will take the CML approach, and this derivation of the MLE follows [37, 30] and the chapter 8 of [36]. The main results including the alternating projection algorithm, Algorithm 2 are being copied in this section for convenience.

8.4.1 Maximum Likelihood Estimator

Recall system model (8.1), the joint probability density function (pdf) of a single snapshot of received data with AWGN is given as

$$f(\mathbf{x_t}) = \frac{1}{(2\pi)^{K/2}|V|^{1/2}} \exp\left(\frac{-(\mathbf{x_t} - A(\theta)\mathbf{s_t})^H V^{-1} (\mathbf{x_t} - \mathbf{A}(\theta)\mathbf{s_t})}{2}\right)$$

Furthermore, owing to assumptions 3 and the noise covariance matrix is symmetric and positive definite, the above multivariate normal pdf can be rewritten as

$$f(\mathbf{x_t}) = \frac{1}{(2\pi)^{K/2}|\sigma^2\mathbf{I}|^{1/2}} \exp\left(\frac{-(\mathbf{x_t} - A(\theta)\mathbf{s_t})^H(\mathbf{x_t} - \mathbf{A}(\theta)\mathbf{s_t})}{2\sigma^2}\right) \tag{8.2}$$

For a sample of L snapshots from the multivariate normal distribution and using assumption 2, (8.2) becomes:

$$f(\mathbf{x_t}) = \frac{1}{(2\pi)^{LK/2}(\sigma^2)^{LK/2}} \exp\left(-\frac{1}{2\sigma^2}\sum_{t=1}^{L}|\mathbf{x_t} - A(\theta)\mathbf{s_t}|^2\right)$$

Since the "log" operator is a monotonically increasing function, maximization of the above likelihood function is equivalent to the maximization of the log-likelihood function. Thus, the log-likelihood function without constant terms is given as

$$L(\theta, S, \sigma^2) = \frac{LK}{2}\log(2\pi) - \frac{LK}{2}\log\sigma^2 - \frac{1}{2\sigma^2}\sum_{t=1}^{L}|\mathbf{x_t} - A(\theta)\mathbf{s_t}|^2$$

Note that there are three unknowns: the noise power σ^2, signal power S and the direction of arrival θ (which is of interest). To maximize the log-likelihood function, we first fix θ and S and differentiate with respect to σ^2, the maximum objective corresponds to the value obtained by equating the differential to zero.

$$\sigma^2 = \frac{1}{LK}\sum_{t=1}^{L}|\mathbf{x_t} - A(\theta)\mathbf{s_t}|^2$$

Substituting the above result back to the log-likelihood function and combining all the constant terms into C', we can write $L(\theta, S, \sigma^2)$ as

$$L(\theta, S) = C' - \frac{LK}{2}\log\left(\sum_{t=1}^{L}|\mathbf{x_t} - A(\theta)\mathbf{s_t}|^2\right) \tag{8.3}$$

Similarly, to maximize (8.3) with σ^2 determined and varying S and θ, the function is maximized with respect to S while keeping θ constant:

$$\max_S L(S) = \min_s \left[\sum_{t=1}^{L}|\mathbf{x_t} - A(\theta)\mathbf{s_t}|^2\right] \quad \text{(By monotonicity of log operator)}$$

This is a LS problem where a well-known solution can be obtained in the following manner:

$$\boxed{\mathbf{s_t} = (A^H(\theta)A(\theta))^{-1}A^H(\theta)\mathbf{x_t}} \tag{8.4}$$

It is at this point to substitute the optimum solution for σ^2 and S into the original objective function and evaluate θ of interest. The final objective function with respect to θ after simplification is shown as

$$\min_{\theta} \left[\sum_{t=1}^{L} |\mathbf{x_t} - A(\theta)(A^H(\theta)A(\theta))^{-1}A^H(\theta)\mathbf{x_t}|^2 \right]$$

where $A(\theta)(A^H(\theta)A(\theta))^{-1}A^H(\theta)$ is the projection matrix, denoted by the projection operator $P_{A(\theta)}$. It represents the projection of $\mathbf{x_t}$ onto the column space of $A(\theta)$. In the absence of noise, and assuming our model is perfect for $A(\theta)$, the column space would span X. However, noise and model errors generally prevent this from happening. In order to estimate θ, we rewrite log-likelihood function to be maximized as

$$\max_{\theta} L(\theta) = \max_{\theta} \left[\text{tr} \left(P_{A(\theta)} R \right) \right]$$

where $R = \sum_{t=1}^{L} \mathbf{x_t}\mathbf{x_t}^H$ is the sample correlation matrix.

Note that, if R is represented by its eigenstructure,

$$R = \sum_{k=1}^{M} \delta(k)\mathbf{u}(k)\mathbf{u}^H(k).$$

Here, $\mathbf{u}(\mathbf{k})$ denotes the k-th eigenvector of R and $\delta(k)$ is the k-th eigenvalue. The log-likelihood function can be rewritten as

$$L(\theta) = \sum_{k=1}^{M} \delta(k)|P_{A(\theta)}\mathbf{u}(k)|^2.$$

An interesting observation is that, unlike MUSIC, the technique under consideration involves all eigenvalues and eigenvectors. We can see the difference later when 3D tomography analysis comes into picture: MLE-AP doesn't produce a beam pattern in the usual sense as MUSIC, yet it only produces M most likely DoAs. The larger the eigenvalue, the more important it is to maximize the projection of the corresponding eigenvector onto the signal subspace.

Sum to all, this is a multi-dimensional nonlinear optimization problem that can be computationally expensive. Moreover, the array manifold can be provided as a look-up table in most cases,

thus making all the conventional gradient type of maximization techniques unapplicable. We will present a computationally attractive method for obtaining the ML estimator in the next subsection.

8.4.2 The Alternating Projection Technique

In this section, we will introduce an efficient computing algorithm, named Alternating Projection, proposed by Ziskind and Wax [37]. It breaks down the problem at hand into a series of alternating maximization problems with a simple technique, and then combines with the projection decomposition scheme. Additionally, it can handle either the case of coherent signals or the case of a single snapshot.

8.4.2.1 Alternating Maximization Technique

The alternating maximization approach is an iterative algorithm: at every step, only one value of θ is estimated while keeping the remaining θ values fixed. Thus, the value of $\theta(m)$ at iteration $h+1$ is obtained by solving the following one-dimensional maximization problem:

$$\hat{\theta}^{(h+1)} = \underset{\theta(m)}{\operatorname{argmax}} \left[\operatorname{tr}(P_{[A(\hat{\theta}^{(h)}),\mathbf{a}(\theta(m))]} R) \right]$$

where $\underset{\theta(m)}{\operatorname{argmax}}$ denotes the value of $\theta(m)$ that yields the maximum value of the objective function. Here $\hat{\theta}^{(h)}$ is a vector of DoAs from the previous iteration, excluding the current DoA for which the function is being maximized, the dimension of which is $M-1$, e.g.,

$$\hat{\theta}^{(h)} = [\hat{\theta}^{(h)}(1), \cdots, \hat{\theta}^{(h)}(m-1), \hat{\theta}^{(h)}(m+1), \cdots, \hat{\theta}^{(h)}(M)], \forall\, h > 0$$

and $\mathbf{a}(\theta(m))$ is the steering vector evaluated using $\theta(m)$ that is to be determined at the current iteration using the above objective function. This technique dooms to generate a local minimum in the end, whether or not it is a global minimum depends on the selection of starting point.

As the initialization step is so crucial to the global convergence of the algorithm, Ziskind and

Wax propose a rather simple, but working excellent procedure as below. It is carried out by assuming a single source scenario, finding the DoA that maximizes the single source result, and then assume two sources, using the output of the single source maximization and performing the maximization again over the newly added source angle, so on and so forth, until all the sources have been estimated. For example,

$$\hat{\theta}^{(0)}(1) = \underset{\theta(1)}{\operatorname{argmax}} \left[\operatorname{tr}(P_{[\mathbf{a}(\theta(1))]}R)\right]$$
$$\hat{\theta}^{(0)}(2) = \underset{\theta(2)}{\operatorname{argmax}} \left[\operatorname{tr}(P_{[\mathbf{a}(\hat{\theta}^{(0)}(1)),\mathbf{a}(\theta(2))]}R)\right]$$
$$\cdots$$
$$\hat{\theta}^{(0)}(m) = \underset{\theta(m)}{\operatorname{argmax}} \left[\operatorname{tr}(P_{[\mathbf{a}(\hat{\theta}^{(0)}(1)),\mathbf{a}(\hat{\theta}^{(0)}(2)),\cdots,\mathbf{a}(\theta(m))]}R)\right]$$

Once the initialization routine is done, we get the estimated source angles ready for iterative alternating maximization technique, and follows by projection decomposition method.

8.4.2.2 Projection Matrix Decomposition

In order to simplify the computational load at every step, the projection update formula is used which is based on a partitioning of the projection matrix. Let B and C be two arbitrary matrices with the same number of rows, and $P_{[B,C]}$ denotes the projection matrix onto the column space of the augmented matrix $[B,C]$. We have

$$P_{[B,C]} = P_B + P_{C_B}$$
$$C_B = (\mathbf{I} - P_B)C$$

Here, C_B refers to the residual of columns of C when projected onto B, which means it is the part of C in the null space of B. This relationship can be applied to simplify the minimization process

as

$$P_{[A(\hat{\theta}^{(h)}),\mathbf{a}(\theta(m))]} = P_{A(\hat{\theta}^{(h)})} + P_{\mathbf{a}(\theta(m))_{A(\hat{\theta}^{(h)})}}$$

$$\mathbf{a}(\theta(m))_{A(\hat{\theta}^{(h)})} = (\mathbf{I} - P_{A(\hat{\theta}^{(h)})})\mathbf{a}(\theta(m))$$

Since the first summand in the projection update formula does not involve $\theta(m)$, it would be sufficient to use only the second summand for obtaining the new updated objective function. This term has a single column containing unknown vector $\mathbf{a}(\theta(m))$, implying that we can calculate its rank-1 projection matrix as $\mathbf{b}\mathbf{b}^H$ using the following unit vector

$$\mathbf{b}(\theta(m), \hat{\theta}^{(h)}) = \frac{\mathbf{a}(\theta(m))_{A(\hat{\theta}^{(h)})}}{||\mathbf{a}(\theta(m))_{A(\hat{\theta}^{(h)})}||}$$

where $||\cdot||$ denotes the Euclidian norm. The objective function can thus be rewritten as

$$\hat{\theta}^{(h+1)} = \underset{\theta(m)}{\operatorname{argmax}} \left[\operatorname{tr}(\mathbf{b}^H R \mathbf{b})\right]$$

Hence, the modified MLE-AP objective function is given by

$$\hat{\theta}^{(h+1)} = \underset{\theta(m)}{\operatorname{argmax}} \left[\operatorname{tr}(\mathbf{b}^H(\theta(m), \hat{\theta}^{(h)})\ R\ \mathbf{b}(\theta(m), \hat{\theta}^{(h)}))\right]$$

Here, we outline the main procedure of alternating projection in Algorithm 2 as below. Note that, the convergence of the algorithm to the global maximum was demonstrated for a variety of scenarios [37], but no solid proof is given. Evidently, the key to this global convergence is the initialization scheme.

Algorithm 2: Maximum Likelihood Estimation By Alternating Projection

Input : Angles look-up table
Output: Estimated Direction of Arrivals
begin
  INITIALIZATION:
  Iteration $h \leftarrow 1$;
  Single source starting $\hat{\theta}^1(1) \leftarrow 0$;
  for $m = 1$ *till* $M-1$ **do**
    $h \leftarrow h+1$;
    $m \leftarrow (m \bmod M)+1$;
    $\hat{\theta}^h(m) \leftarrow \hat{\theta}^{h-1}(m)$;
    $\hat{\theta}^h(m) \leftarrow \underset{\theta(m)}{\operatorname{argmax}} \left[\operatorname{tr}(\mathbf{b}^H(\theta(m), \hat{\theta}^{(h)})\ R\ \mathbf{b}(\theta(m), \hat{\theta}^{(h)}))\right]$;
  end
  MAIN LOOP:
  while $|\hat{\theta}^h - \hat{\theta}^{h-M}| > \varepsilon$ **do**
    $h \leftarrow h+1$;
    $m \leftarrow (m \bmod M)+1$;
    $\hat{\theta}^h(m) \leftarrow \hat{\theta}^{h-1}(m)$;
    $\hat{\theta}^h(m) \leftarrow \underset{\theta(m)}{\operatorname{argmax}} \left[\operatorname{tr}(\mathbf{b}^H(\theta(m), \hat{\theta}^{(h)})\ R\ \mathbf{b}(\theta(m), \hat{\theta}^{(h)}))\right]$;
  end
end

Chapter 9

Dataset Analysis

As illustrated in [31, 29], we can apply direction of arrival methods to avoid left-side and right-side ambiguities with multiple phase centers in the cross-track dimension. Additionally, with pulse compression providing time-delay resolution and azimuth processing providing along-track resolution, 3D basal imaging is possible. Here, we only focus on the application of DoA techniques to combine the SAR processed data from different channels to produce a single tomographic image. When the target's along-track position, time delay information and DoA distribution are known, we can geocode the three parameters to obtain the corresponding along-track position, cross-track position and elevation of the target. The following sections present the 3D tomography results for a dataset taken during the 2013 Greenland campaign and show our method works successfully to estimate the ice bed height.

9.1 Application of Algorithms

Each of the algorithms illustrated in the previous chapter is applied to a SAR processed image to obtain the DoAs that is in turn used to derive the cross-track and elevation values necessary for geocoding the target. In this section, we mainly discuss how to improve the performance of the MLE-AP algorithm when applying it to our dataset, e.g., by replacing ideal steering vector generation with measured steering vectors, automatic determination of the number of backscattered

sources, smoothing the 3D topography in order to get a more accurate height estimation, introducing quality metrics associated with estimated points and how to speed up the MLE-AP routine while maintaining the same accuracy, etc.

9.1.1 MUSIC

The estimation performance of the MUSIC algorithm depends heavily on the estimation of the sample correlation matrix (SCM) of the input, which in this case is acquired by samples from closely spaced along-track positions at the antenna array [30]. In our situation, we made an assumption that the targets and sensors are stationary for the time and spatial spans over which the observations are made, which is reasonable for a smooth ice bottom. With a sample support of 11 and the number of sources of 2, the approximation of the SCM is modest reliable. The sample support comes from eleven closely spaced along-track positions, five to the left and five to the right of the current position. The 2 comes from the assumption that there are two dominant sources, one to the left and the other to the right of nadir. Later in subsection 9.1.2.2, we will use model order statistics to automatically determine the number of sources from the preprocessed data, rather than fixing it to 2. But for the rest of the thesis, unless we mention otherwise, we set the number of sources to 2.

Generally, for determining the peak values, the top two eigenvalues (two assumed sources) are used to determine the signal plus noise subspace. However, in our case, we produce a continuous cepstrum using MUSIC. Here, we divide the frequency range from $-\pi/2$ to $\pi/2$ into 181 equally spaced spatial-frequency bins, which sufficiently over-sample the result so that no additional improvement is available by increasing the number of bins.

9.1.2 MLE-AP

The MLE-AP technique is an efficient method to break down the complex multivariate optimization problem into a sequence of much simpler 1D optimization problems. It is iterative and we need to set a stopping criterion for termination. In our implementation, the algorithm is terminated

if the difference between the current set of results (DoA estimation) and the previous set is less than 1.

MLE is generally considered better than the MUSIC algorithm in terms of DoA estimation [37]. Although the essence of our problem is a DoA estimation problem, for the sample dataset and particular tomographic application, the surface extraction routine of MUSIC outperforms the surface extraction routine of MLE (we will show this later in section 9.2). This is because for our specific surface extraction routine, MLE tends to suffer worse when the peak DoA is wrong and produces large errors in the elevation data. Note that the basal result obtained from MUSIC is extracted from the continuous cepstrum, a beam pattern that has a value for every angle of arrival and sources are distinguished by large/small values. On the other hand, MLE extracts the bottom information from the two best sources (in terms of the likelihood function value) rather than a complete beam pattern. This may contribute to the deterioration of the MLE results relative to the MUSIC results because when the algorithms are wrong, MUSIC may still have a small peak at the correct location whereas MLE will return no data at the correct location. In this subsection, we will introduce some post-processing procedures to improve the performance of the MLE-AP algorithm.

9.1.2.1 Measured Steering Vectors

We used data collected over a relatively flat surface (ocean) to create a set of measured steering vectors. We assume that, on average, the peak return is from nadir or directly beneath the aircraft so that the DoA is known a priori. The plane is rolled back and forth $+/-45$ deg during the measurements. Since the peak return is always from the nadir, the peak return's direction of arrival relative to the broadside of the antenna array sweeps $+/-45$ deg and using the roll data that is collected by the inertial navigation system (INS), we can collate each peak return received by the array with a specific direction of arrival. To be specific, if the aircraft is rolled at 30 degree and the target is at nadir, that gives a measurement of the steering vector for -30 degree. From these measurements, we generated a steering vector look-up table for $+/-45$ deg. Thus, during processing, the measured steering vector look-up table will be used to estimate the actual complex

steering vector (instead of the ideal one) based on the roll information of the aircraft.

The procedure for creating the steering vector table is as follows. First, the data are coherently averaged (unfocussed SAR processing) to help focus the beam downward and increase the signal to noise ratio. Next the data are pulse compressed. We then synchronize the radar data with the INS data so that we know the roll angle for each range line (record). For each range line of data we extract the complex values associated with the peak return for each array element and form this into a vector. This vector is one snapshot of data across the array for a nadir target. We do this for each range line of data collected. We then sort these snapshots according to the aircraft roll angle at the time the snapshot was taken. Normally there are thousands of range lines corresponding to various different roll angles. In order to reduce the effects of noise and errors in our assumption that the scattering target is always at nadir, we divide up the roll angles into one-degree wide bins and average all the results in each bin to get a single result for each angle. When we need to generate complex steering vectors, we perform linear interpolation using the values from the look-up table according to the specific roll angle.

To create the steering vectors, we take the center antenna as the reference (we have seven antenna elements). The angles at nadir are forced to match the ideal case at nadir as indicated in Fig. 9.1(b). The reason is the receiver equalization that is performed on the dataset during SAR and array processing insures the condition that the steering vector at nadir matches the ideal case (i.e. equalization is done so that the ideal case at nadir is met). Then a median filter is applied to smooth the curve and reduce point errors. Next we phase unwrap the data to make the curve continuous for plotting purposes. Finally, we generate the steering vectors look-up table by interpolating the existing information to the range of -45 to 45 degrees.

Fig. 9.1(a) shows the angle of the complex ideal steering vectors for the seven element array that we performed this procedure on. The array is conformal to the bottom of the aircraft fuselage and so is not quite linear. That is why there is some offset for each channel in the nadir direction as shown in Fig. 9.1(a). Fig. 9.1(b) is the result of a combination of ideal and measured steering vectors; measured angles are used from -45 to 45 and ideal angles are used outside this region.

A discontinuity can be seen at the transition between the ideal and measured steering vectors. We would like to use the measured steering vectors for angles from -45 to 45 deg and the ideal steering vectors outside this region, but we need to correct the gap in order to make the angle distribution continuous on the whole range. A corrected version is shown in Fig. 9.2(a) where the gap is closed

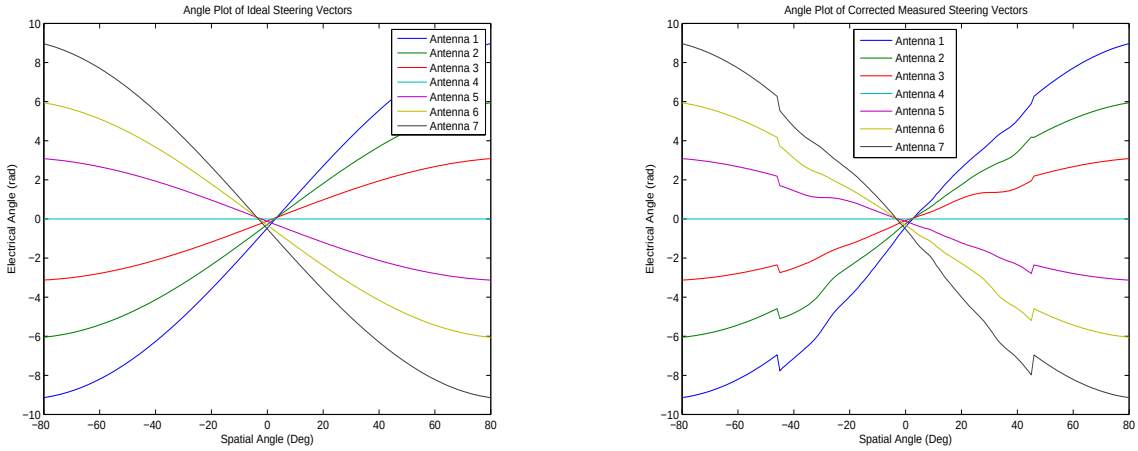

(a) Angle Distribution of Ideal Steering Vectors Generation

(b) Angle Distribution of Combined Ideal and Measured Steering Vectors Generation

Figure 9.1: Angle Distribution of Steering Vectors for Multi-channels

by adding an offset to the ideal steering vectors to make them continuous. The difference between angles of ideal and corrected measured steering vectors can be seen in Fig. 9.2(b). Actually, in the nadir direction, there should be no difference between ideal and corrected measured steering vectors. But we do a moving-average smoothing to make the line continuous and this leads to the difference in the nadir direction of Fig. 9.2(b). We show the smoothed magnitude information in Fig. 9.3 in log scale. Note that, the ideal steering vector magnitude is one for all angles. Hence the magnitude value of complex steering vectors outside -45 to 45 is constant. We will use both ideal and measured steering vectors during array processing and a comparison of the results is given in section 9.2.

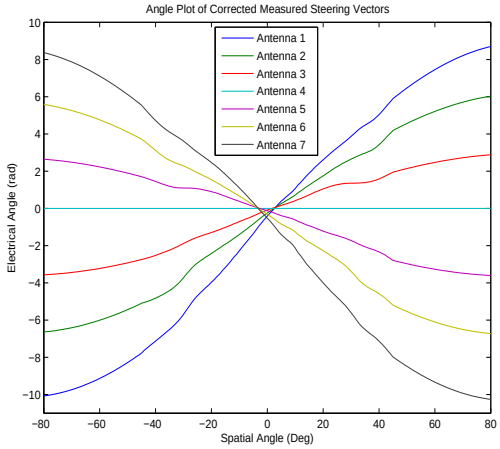

(a) Angle Distribution of Corrected Measured Steering Vectors Generation

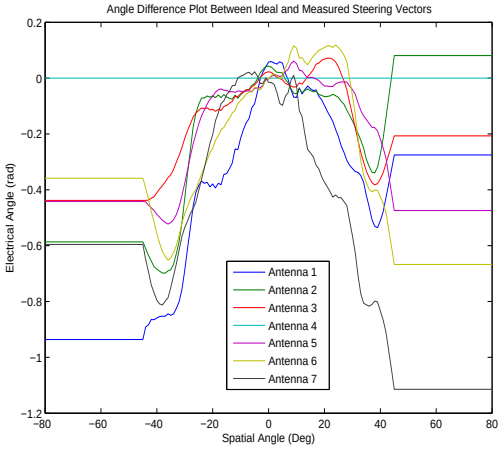

(b) Angle Difference Between Ideal and Corrected Measured Steering Vectors Generation

Figure 9.2: Angle Distribution and Difference of Steering Vectors for Multi-channels

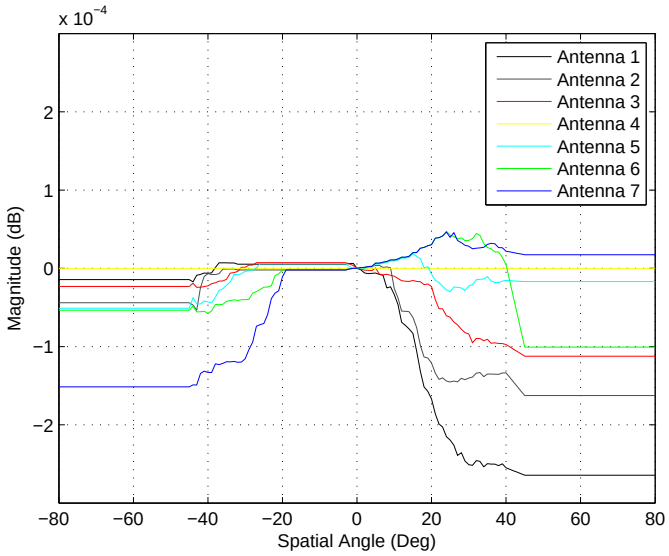

Figure 9.3: Magnitude Distribution of Corrected Measured Steering Vectors Generation

9.1.2.2 Model Order Statistics

As noted by Raghunandan [30], when the two source model is not applicable (e.g., because of surface clutter), the use of model order statistics can be very useful. Indeed, we can show the advantage when the number of sources can be determined automatically using information theoretical approaches in section 9.2.

The observed or measured data can be modelled as the superposition of a finite number of signals with additive noise. An accurate estimate of the number of sources is essential in many signal processing problems such as in the DoA estimation by a smart antenna system, in the poles retrieval of a system response, and in image processing. Early on, Bartlett proposed a hypothesis testing procedure to test the signals by likelihood ratio statistics with pre-determined thresholds. But the actual distribution of the test statistics can only be approximated and a choice of the level of significance is required [38]. Approaches based on information criterion are becoming more popular because of their accurate estimation performance. Two commonly used model selection criteria are: Akaike Information Criterion (AIC), and Bayesian Information Criterion (BIC), which is also named as Minimum Description Length Criterion. The number of signals for both criteria is determined by simply minimizing the value of an information criterion. Many variations of these two criteria have been proposed. However, they are existing benchmarks commonly used in model selection problems in time series and regression analysis.

Given the observed data and a set of candidate probability models that depend on the parameter vector Θ (including the eigenvalues and eigenvectors of the sample correlation matrix and noise power), a model selection criterion selects the model order by minimizing a loss function and can be expressed in the following form [38]:

$$\text{A model selection criteria} = -2\log L(X|\hat{\Theta}) + P(L,k_p) \tag{9.1}$$

where $L(X|\hat{\Theta})$ is the likelihood function, $\hat{\Theta}$ denotes the maximum likelihood estimate of Θ, L is the sample size and k_p is the number of freely-adjusted parameters (degrees of freedom) in Θ, which is a function of both p and q. p is the number of nonzero eigenvalues and q is the number of sources. The first term is a measure of the goodness of fit of the candidate model to the data. The second term serves as a penalty term for over fitting.

AIC can be obtained when the penalty term in (9.1) is set to be $2k_p$ [36],

$$\text{AIC} = -2\log L(X|\hat{\Theta}) + 2k_p \tag{9.2}$$

while for BIC, the penalty term is $k_p \log L$,

$$\text{BIC} = -2\log L(X|\hat{\Theta}) + k_p \log L \tag{9.3}$$

where $k_p = q(2p-q)+1$. The estimation performance can be effected by the actual number of signals, signal strength, signal separations, signal correlations, number of snapshots, etc. In our application, the 11 closely spaced along-track snapshots may correlate with each other, and 11 is a modest sample support. Thus we tend to choose BIC as our model order selection criterion since BIC is consistent, showing great performance when incoming signals are correlated and conquering the overestimation problem with AIC.

Note that, the expected number of signals in the data is two for ice bottom tomography without surface clutter. With ice surface clutter, we would expect 4 signals to handle left and right clutter. We assumed that there were no other sources of energy, although there is some possibility that RFI or englacial targets may be present at times. Hence, we constrain the number of sources estimated to be $2, 3$ or 4. To test the efficacy, we used the fixed two sources model and automatically-determined number of sources model to initiate the DoA estimation procedure. Performance comparison plots can be seen in section 9.2.

9.1.2.3 Bottom Smoothing

As illustrated in section 8.2, our dataset is actually a point cloud (MLE) consisting of thousands of slices in the along-track dimension, and targets are resolved to each slice through SAR processing. To simplify the problem, we fix the number of sources to two again in accordance with our system model plot: one on the left and the other on the right. Our final goal is to improve height estimation and obtain an artifact free 3D tomography image, in order to create a more accurate DEM.

For either approach (MUSIC or MLE), each voxel in our matrix is assigned a scattering value during signal processing. Generally, if there is no scattering target (i.e., ice bottom) in the voxel,

then the scattering value is small because only system noise contributed and we can discard these points by a simple threshold method. In this way, most of the points are removed. However, in some cases, because the noise is random and has a non-zero probability of being large at times and we are often trying to see weak scatter targets, the threshold method is not sufficient. Here, we would like to use a priori knowledge that we are imaging a slowly changing surface and mask bad points out using this additional spatial knowledge as well.

The output data from the array processing routine is subjected to some post-processing steps. Originally, the surface extraction routine for MLE is conducted as below. We first do an interpolation of layer data defined by hand-picked surface and bottom values that used the traditional 2D imagery. Through the surface and bottom information, we calculate an approximate range for where the ice bottom would lie, which is the "mask". The width of the mask is programmable. Then we search for the maximum value in each cross-track frequency bin and keep track of which range bin the maximum falls in. Using the tomography toolbox by Paden et al. [31], we find a polynomial based function which converts time-delay to target (x coordinate), and direction of arrival to a cross-track (y coordinate) and elevation position (z coordinate). In the end, we convert geocentric data values to a geodetic coordinates, which means transform the (x,y,z) data into a tuple of latitude, longitude and elevation. The 3D imaging of DEM is possible. We show the 2D cross-track image for the original surface extraction routine of MLE in Fig. 9.4. The points in the plot indicating the estimated ice bottom, which do not form a continuous line.

In our thesis, the modified surface extracting routine we have implemented seems to work well and involves outlier filtering, maximization, interpolation and smoothing. These steps are incorporated after the third step of original surface tracking routine (i.e. the maximum finding). We use frame 20130410_01_033 from the 2013 Greenland P3 campaign to illustrate the denoising procedure. The output figures display the distribution of the directions of arrival in terms of the estimated relative signal power by these two algorithms. Note that, the MUSIC cepstrum does not technically represent signal power, but is generally correlated to it.

Fig. 9.5(a) is an example of a single slice from the point cloud. We can see a lot of points

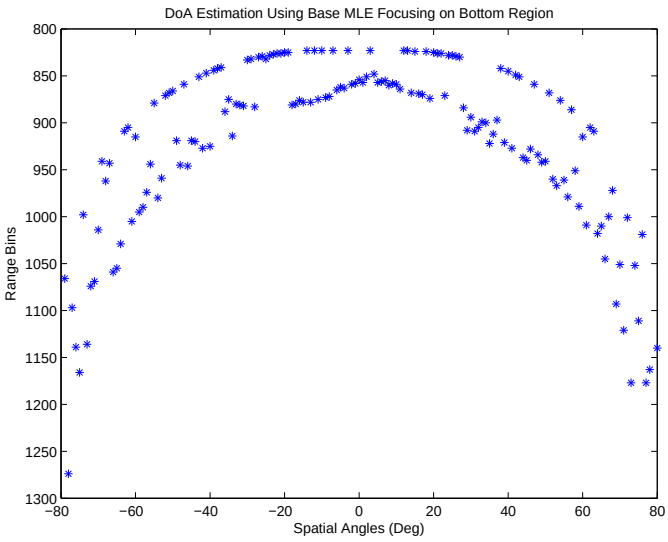

Figure 9.4: DoA Distribution Using MLE Focusing on Bottom Region.

indicating the internal ice layers and ice bottom echoes and clutter (the ice surface is not visible since it was received while the receiver blanking switch was on). It is easy to distinguish out the ice bottom by eye, which is the region starting from range bin 850 and ending with about 1000 (a continuous line). However, if we zoom in to this bottom region, many discontinuities can be seen as shown in Fig. 9.5(b). First, a quick observation about the shape of the basal scattering in Fig. 9.5. For a flat surface and not taking into account the ice medium, the range versus incidence angle θ is:

$$\text{range} = \frac{z_0}{\sqrt{1-\sin^2(\theta)}} \tag{9.4}$$

where z_0 is the height of the plane above the surface. This shape resembles a parabolic shape which goes to infinity as θ goes to $+/-90$ deg. In other words, if we transform to rectangular coordinates, the basal scatterers in Fig. 9.5 would be a horizontal line if the surface was perfectly flat. Now, if the intersection of the slice with the ice bottom always gave a positive return and the ice bottom was continuous, we would expect a continuous line of scatterers which looks somewhat parabolic with deviations caused by the ice bottom topography.

Since the surface does not produce a continuous line because of errors in the angle of arrival

estimates, we try to apply interpolation to fill up those discontinuities. First, we need to make sure every frequency bin only has one good position value. If there is more than one position value in a frequency bin, we take the mean of them. If there are no good position values for a bin, we denote it as NaN. After the simple filling up procedure, we apply the outlier detection to avoid bad samples distorting the data before interpolation. As assumed earlier, the ice bottom is slowly changing. Thus large jumps between range bin values of adjacent frequency bins would be considered as outliers. Here, we set the threshold to be 50, which means if any two adjacent positions have a difference over 50, then it will be regarded as bad data and replaced with NaN. At this point, we will fill in the gaps with linear interpolation between good values as follows:

$$\text{value(index)} = \text{prev}_{\text{value}} + \frac{(\text{next}_{\text{value}} - \text{prev}_{\text{value}}) \times (\text{index} - \text{prev}_{\text{index}})}{(\text{next}_{\text{index}} - \text{prev}_{\text{index}})} \tag{9.5}$$

where index is the current direction of arrival angle index, value is the range bin position belonging to the corresponding angle. $\text{prev}_{\text{value}}$ and $\text{next}_{\text{value}}$ indicate the previous and next existing range bin position for the current angle index, respectively. Similarly, $\text{prev}_{\text{index}}$ and $\text{next}_{\text{index}}$ represent the previous and next angle index where there exists range bin good position values. A scatter plot regarding range bin position for each angle index is shown in figure 9.5(c). In the end, the "Savitzky-Golay" method [39] is applied to smooth the result because of its ability to smooth the data without greatly distorting the signal. Its principle is to fit successive sub-sets of adjacent data points with a low-degree polynomial by the method of linear least squares. The resulting smoothing performance is shown in figure 9.5(d) as the red line, while comparing to the blue asterisks representing the un-smoothed bottom.

In section 8.4.1, we noted that MUSIC and MLE are different when you break them into their respective eigenstructures. Also, MLE just produces two discrete angle estimates (one from the left and one from the right) as opposed to MUSIC, where the cepstrum that is used has a value for every direction of arrival and sources are distinguished by large values. Hence, MUSIC produces a smooth angular distribution compared to MLE. This is because when MLE gets the wrong scatter

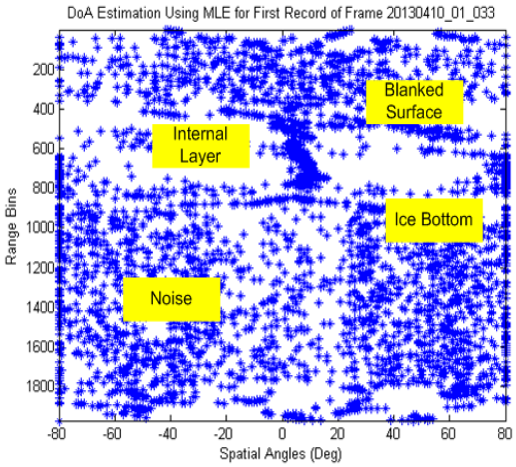

(a) DoA Distribution for the Whole Elevation Dimension

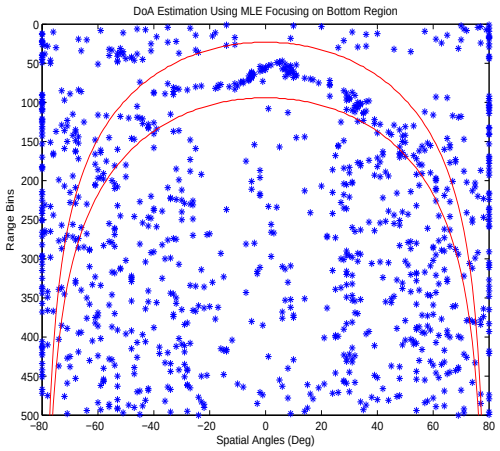

(b) DoA Distribution Zoom in Bottom Region With Guard Lines

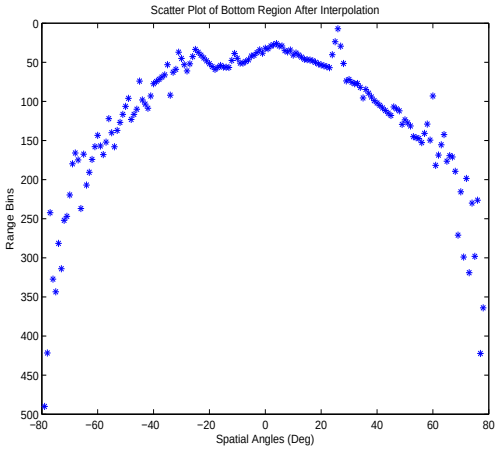

(c) DoA Distribution After Interpolation

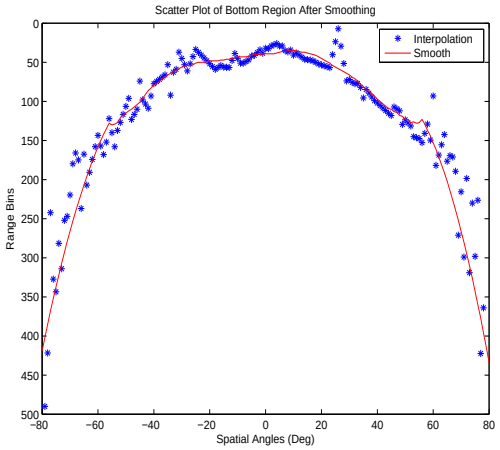

(d) DoA Distribution After Interpolation and Smoothing

Figure 9.5: DoA Estimation Using MLE for First Record of Frame 20130410_01_033

location (e.g. because the ice bottom SNR has dropped too low), we might get a point target with a large angular error whereas the MUSIC cepstrum will tend to still have some peak near where the ice bottom actually is (although it might not be one of the two dominant peaks). This can be seen in the comparison between Fig. 9.5(b) (MLE) and Fig. 9.6 (MUSIC), the expected mask ("the range between two red lines") is trying to restrict the tracing region of ice bottom. We regard peaks outside this region as bad data. As highlighted in Fig. 9.6 for MUSIC, there may be peaks outside the mask, but the neighbourhood region still contains a peak. But for MLE in Fig. 9.5(b),

if a peak is outside the mask region, we totally lose the information related to this estimate. That is the reason why the base surface tracking routine of MUSIC performs better than the base routine of MLE.

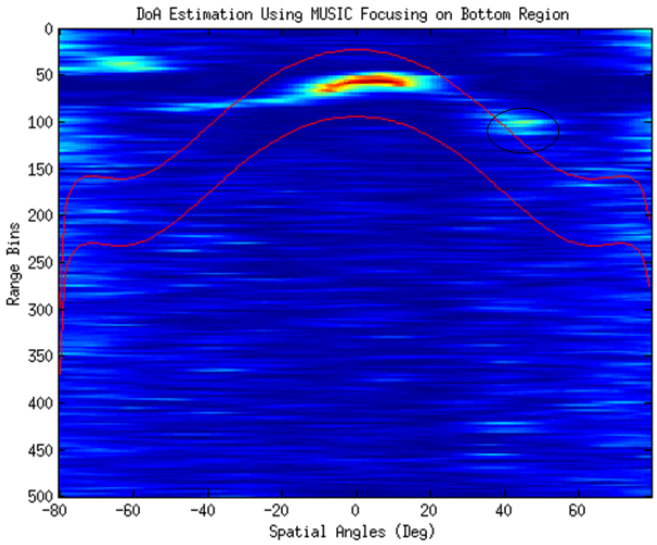

Figure 9.6: DoA Distribution Using MUSIC Focusing on Bottom Region.

9.1.2.4 Speed Up MLE-AP

The processing time is an important metric we should take into account. Though we utilize the computationally attractive alternating projection method to compute the multi-dimensional ML estimator, it is still much slower than the MUSIC algorithm. As discussed in [30] and our data processing procedure, MUSIC takes 0.5s to process one range line while MLE needs 22.64s. Normally, the point cloud contains thousands of range lines, which means MLE is thousands of times slower than the MUSIC algorithm. Indeed, this is the case, for one data frame, MUSIC only needs 2 minutes while MLE takes almost six hours. We still need to speed it up without decreasing the spatial resolution.

If we set the spatial resolution to 1 degree (that is 181 equally spaced spatial-frequency bins), we need 181 operations to get the maximum. However, note that, for an airborne-radar with only seven antenna elements, we don't need this level of accuracy to find the approximate location of

the global maximum, especially for the initialization step in the MLE-AP algorithm. Hence, we can do a sparse grid search followed by function optimization. For example, we first loosen the angle steps from $-90:1:90$ to $-90:5:90$ and conduct the initialization step. After determining which range bin the maximum falls into, say 36, we tighten the angle range again around 36, which is $30, 31, \cdots, 36, 37, \cdots, 40$. In this manner, we maintain the resolution to be 1 degree, but the number of operations effectively reduced from 181 to 48, almost four times less work load. Actually, the loose grid size can be programmable. Through implementation, the running time for one range line decreases in half, from 22.64s to 11.55s. And the total running time for one data segment reduce from 6 hours to around 1 hour. Moreover, the performance of 3D tomographic cross-over analysis is as good as before.

9.2 Output From Greenland Dataset

The data frames used for the comparison of the algorithms are 20130404_02_040 and 20130410_01_033. These crossing flight lines were collected near Jakobshavn Glacier in southwestern Greenland. The flight pattern and echograms are illustrated in Fig. 9.7. Fig. 9.7(a) and Fig. 9.7(b) are the flight paths for the two data segments, while Fig. 9.7(c) and Fig. 9.7(d) draw the flight pattern of these two days together with the highlighted lines corresponding to the specific data frames of interest. The radar echograms for these two data frames are shown in Fig. 9.7(e) and Fig. 9.7(f) respectively. These radar echograms are made by forming a fixed beam at nadir with the array where the vertical dimension is elevation and the horizontal dimension is along the aircraft's flight trajectory.

These two data frames were chosen because they cross each other in a region where the ice bottom is rough enough to backscatter sufficient energy to the radar that can be used to form a DEM. Although we do not know the actual ice bottom elevation, we know that the algorithms should be self consistent. Since it is impractical to determine the actual elevation, we compare the algorithm produced DEMs from the two crossing lines and assume that a lower mean squared error between the DEMs means that the algorithm is performing better (i.e. it is more self consistent).

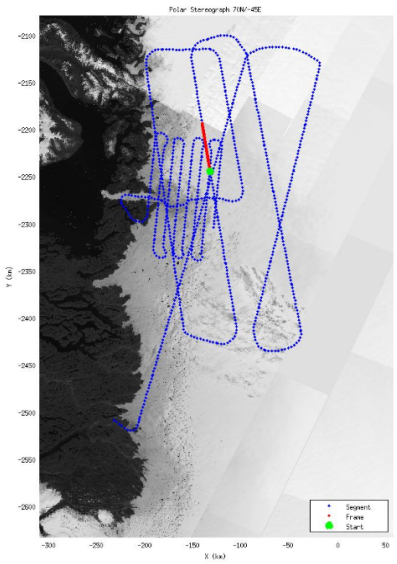

(a) Flight Path for Segment 20130404_02_040

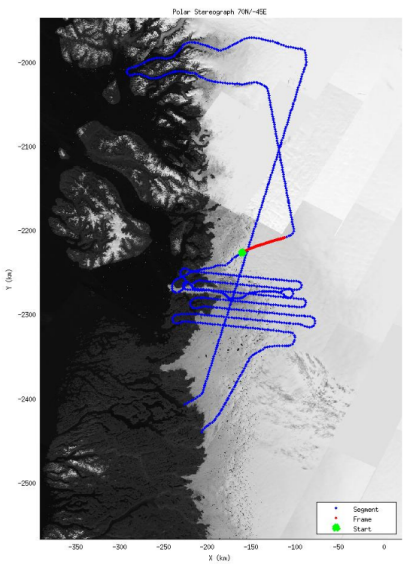

(b) Flight Path for Segment 20130410_01_033

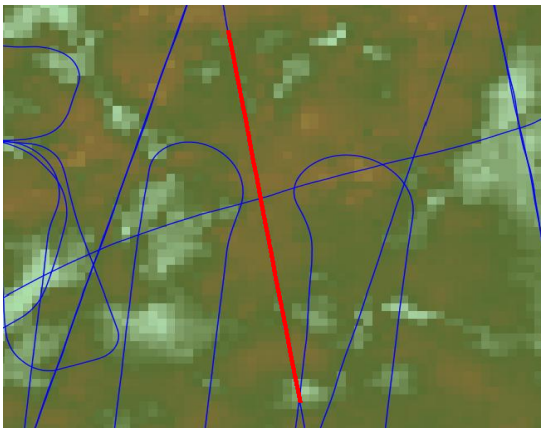

(c) Flight Pattern for Cross-over Analysis of Data Frame 20130404_02_040

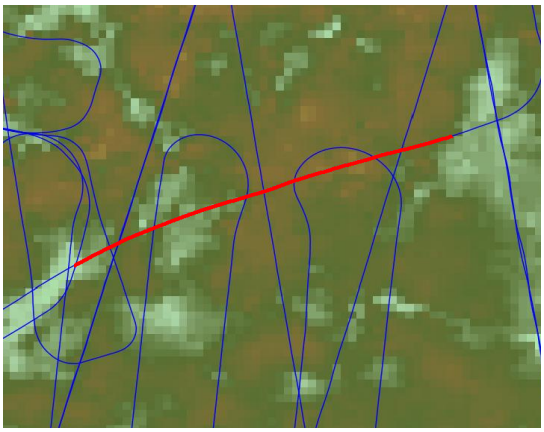

(d) Flight Pattern for Cross-over Analysis of Data Frame 20130410_01_033

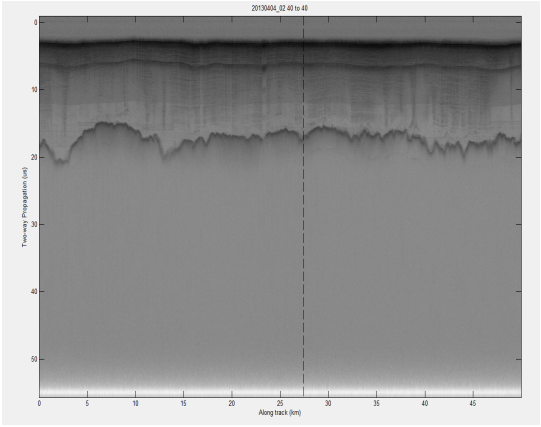

(e) Echogram of Data Frame 20130404_02_040

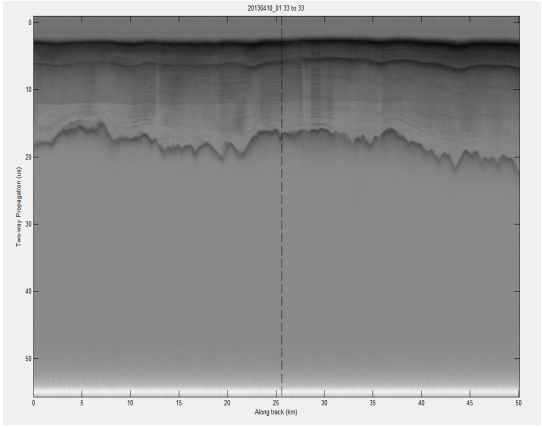

(f) Echogram of Data Frame 20130410_01_033

Figure 9.7: Flight Pattern and Echograms

Here, we will first show the results by the surface tracking routine of MUSIC as a benchmark, then implement different modifications to the surface extraction routine of MLE-AP algorithm described in section 9.1.2. Fig. 9.8 below shows the estimate of 3D topography from the base of the ice sheet using an ice sheet propagation model to geocode the results [31]. The cross-track width of the topography swath is 750m on each side of the radar.

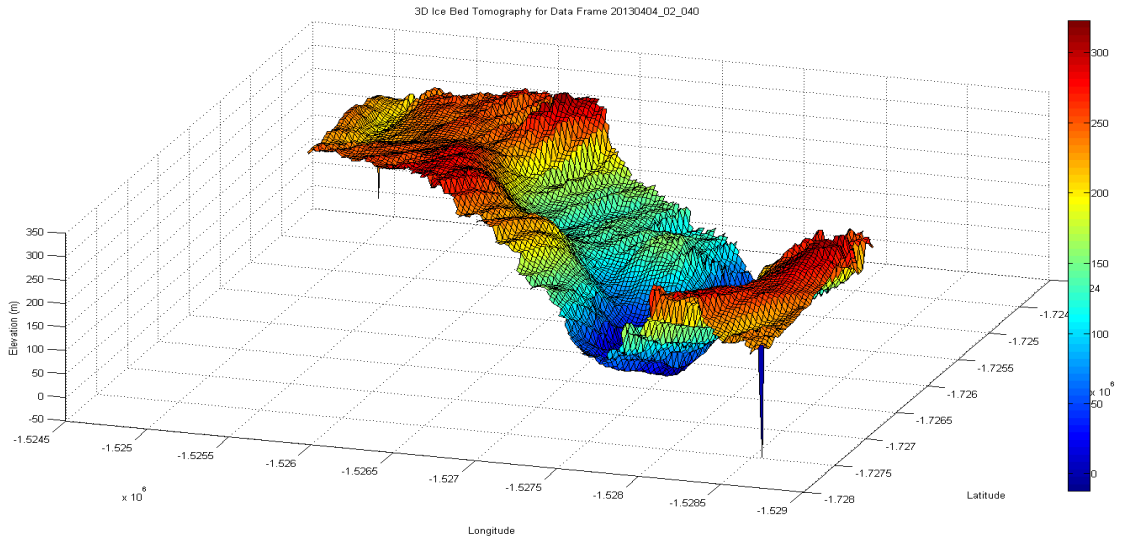

(a) Subsection of Data Frame 20130404_02_040

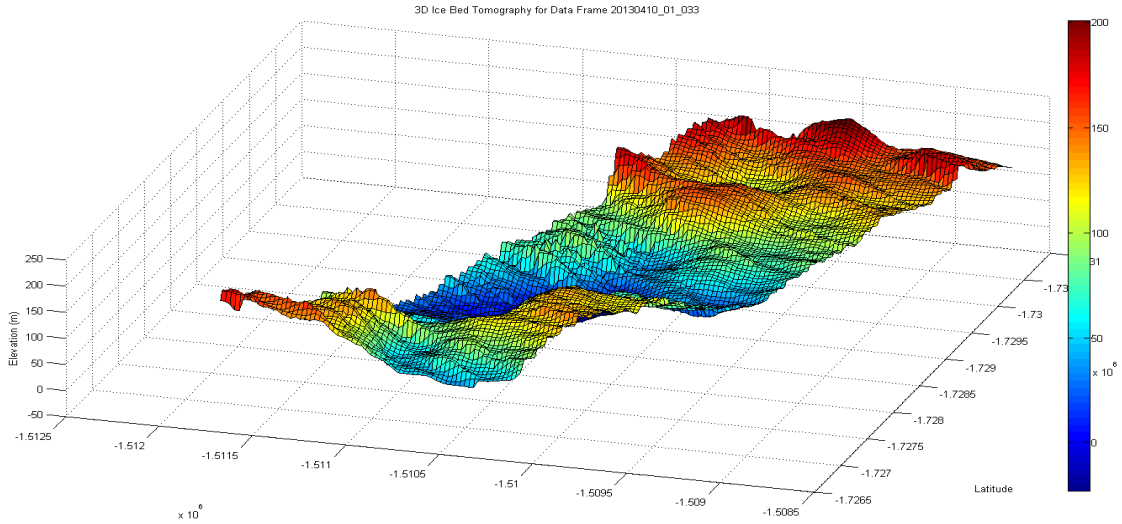

(b) Subsection of Data Frame 20130410_01_033

Figure 9.8: DEM From a Single Pass Using the MLE Algorithm

In Fig. 9.9, the cross-over region of these two frames is presented. We can see clearly that there exists a valley in the middle of the plot, just as indicated by the little hollow in Fig. 9.7(e) and Fig. 9.7(f) where the dashed lines lie. The two plots match very well, and we can confirm that this is indeed the overlapping region. The difference statistics between the two DEMs, mean (MEAN), standard deviation (STD) and root mean squared error (RMSE), are shown in Table 9.1 for comparison.

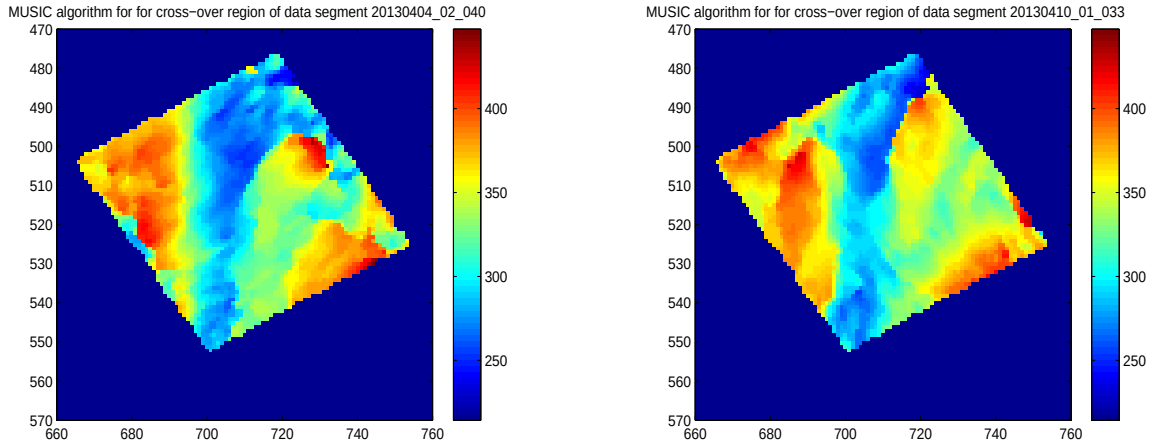

(a) Data Frame 20130404_02_040

(b) Data Frame 20130410_01_033

Figure 9.9: Cross-Over Analysis by MUSIC

As for MLE-AP, if we directly apply the algorithm without bottom smoothing, the results are poor as shown in Fig. 9.10. It is very hard to tell that these two plots are for the same overlapping region, because they don't really look the same. Throughout the whole experimental process, we found that bottom smoothing is the crucial step to improve the performance of the surface tracking routine of MLE-AP algorithm. Without it, the plots will be messy because MLE always produces some artifacts. After our denoising routine, we can see the results in Fig. 9.11, which match very well with the benchmark produced by the MUSIC algorithm. The valley clearly shows up again.

The next step is to replace ideal steering vectors with the measured steering vectors look-up table. The results are shown in Fig. 9.12. The cross-over plots using model order statistics are given in Fig. 9.13. We can see no big difference between Fig. 9.11, Fig. 9.12 and Fig. 9.13. Moreover, from the statistics comparison in Table 9.1, we can see that the results produced by measured

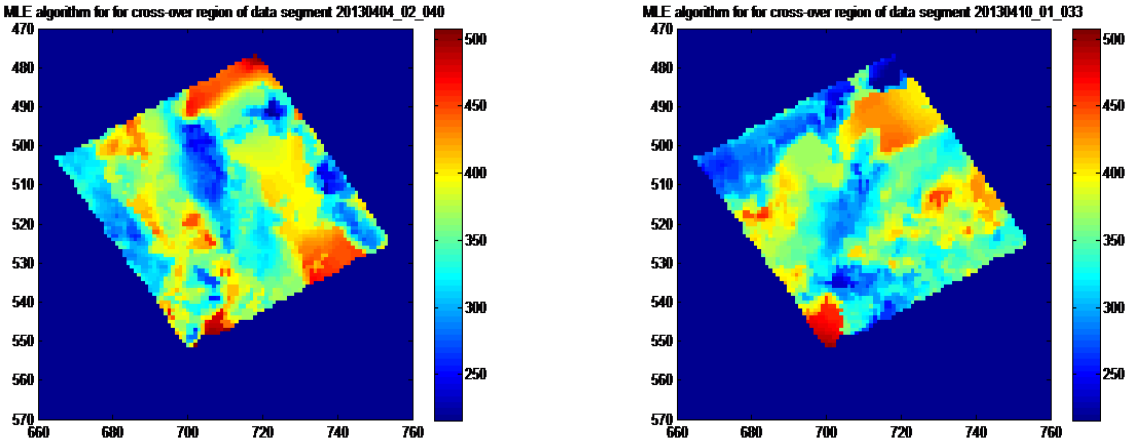

(a) Data Frame 20130404_02_040 (b) Data Frame 20130410_01_033

Figure 9.10: Cross-Over Analysis by MLE Without Bottom Smoothing

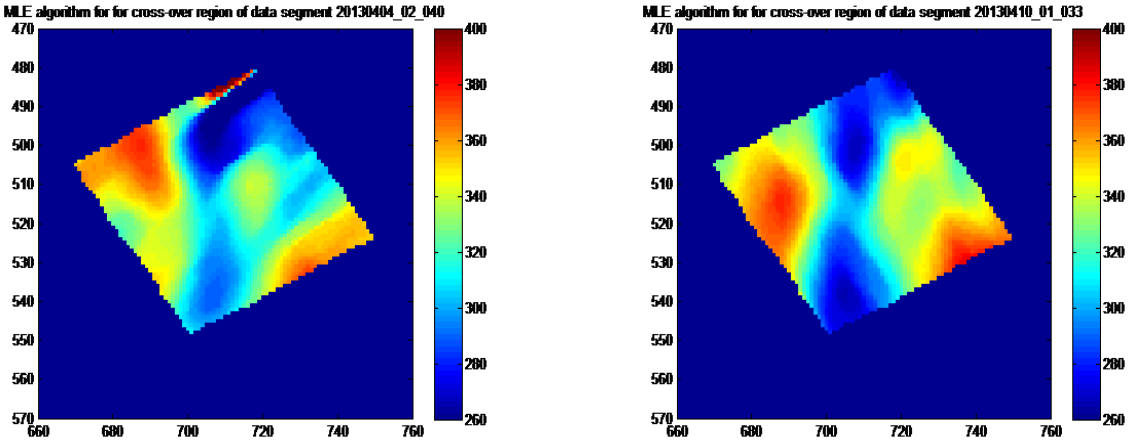

(a) Data Frame 20130404_02_040 (b) Data Frame 20130410_01_033

Figure 9.11: Cross-Over Analysis by MLE With Bottom Smoothing

steering vectors and model order statistics application are even worse than that of the original MLE-AP algorithm with bottom smoothing, in terms of the MEAN, STD and RMSE. There are a number of possibilities of why the modifications do not improve the performance as they aim to. First, there could exist errors during the estimation process of the steering vectors of the model order statistics. For example, we collect the data over the ocean and assume the surface is relatively flat, but waves will cause the dominant reflection to not always be at nadir. Additionally, during the process of generating the complex steering vector look-up table, we have done averaging, median

filtering, interpolation and smoothing. Each routine will probably reduces noise, but also lowers the resolution of the steering vector estimation. Finally, we only test one dataset and it is not a sufficiently large sample to say that either of these routines failed or succeeded in improving the MSE in general.

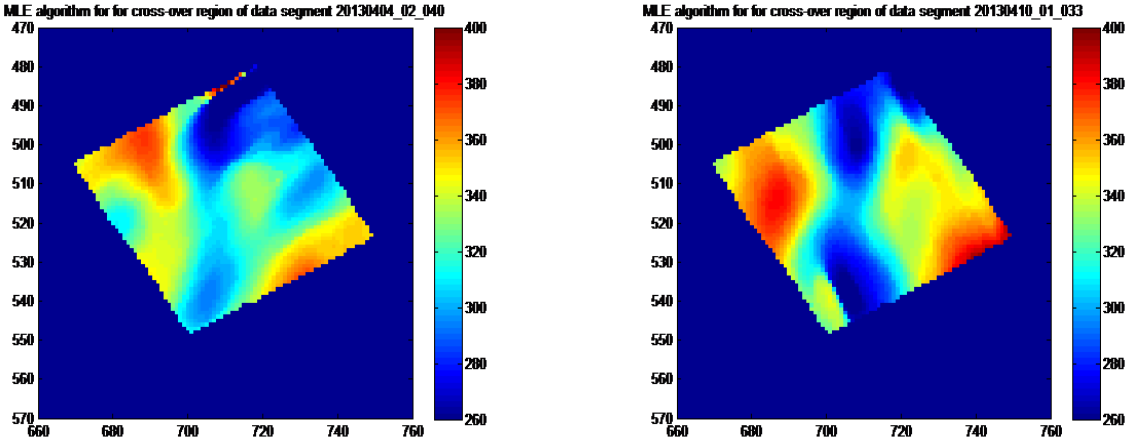

(a) Data Frame 20130404_02_040 (b) Data Frame 20130410_01_033

Figure 9.12: Cross-Over Analysis by MLE With Measured Steering Vectors

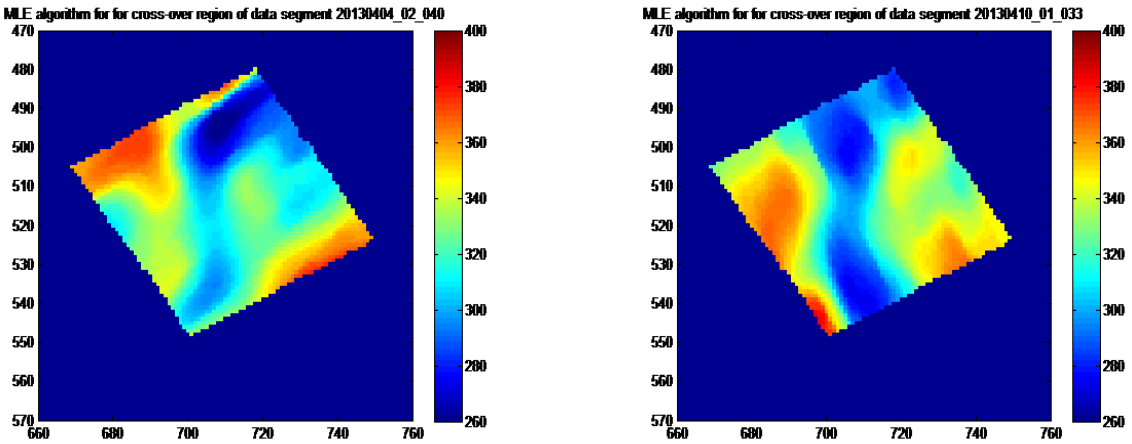

(a) Data Frame 20130404_02_040 (b) Data Frame 20130410_01_033

Figure 9.13: Cross-Over Analysis by MLE With Model Order Statistics

The final step is to incorporate quality metrics into the culling process, i.e., backscattered signal strength and the likelihood value of the objective function. A bigger value of backscattered signal

spectrum indicates a greater possibility that there exists a target. Similarly, the larger the likelihood value, the more confident we are that the target lies in that angle bin. This is an effective procedure to mask out the artifacts made by MLE.

To do this, we remove bad points if they fall below a threshold backscattered signal strength and/or the likelihood objective function value. We first show the backscattered signal power distribution of the overlapping region in Fig. 9.14(a) and 9.14(b). Since the values cover a wide dynamic range, log-scaled plots are presented. We set the bad point threshold to be -75, which means any backscattered power value less than -75 will be considered an artifact and be masked out from the cross-over plots. We chose -75 as the threshold because it gave the best cross-over performance. The results can be seen in Fig. 9.14(c) and Fig. 9.14(d). The difference results are only slightly improved and are given in Table 9.1. We also test the likelihood value metric, but the difference result is similar. This makes sense, since the distribution of the likelihood value in Fig. 9.15(a) and Fig. 9.15(b) is very similar to the backscattered signal power shown in Fig. 9.14(a) and Fig. 9.14(b).

Table 9.1: Difference Statistics Comparison between MUSIC and Various Applications of MLE-AP Algorithm

Algorithm	MEAN	STD	RMSE	MAX DIFF	MIN DIFF
MUSIC	20.33	21.93	29.90	143.50	0.0017
MLE-AP	62.86	47.62	78.86	286.92	0.0146
MLE-AP WITH SMOOTHING	17.62	14.98	23.13	162.79	0.0056
MLE-AP WITH MEASURED	20.23	14.87	25.43	158.31	0.0094
MLE-AP WITH MODEL ORDER	19.64	14.79	24.58	76.13	0.0078
MLE-AP WITH QUALITY METRIC	18.52	14.06	23.25	76.13	0.0078

From the statistics of Table 9.1 (MAX DIFF and MIN DIFF indicate the maximum and minimum difference value between two single pass images, respectively), we can see that after bottom smoothing, the surface extraction routine of MLE-AP indeed performs better than the surface extraction routine of MUSIC. All three criteria are lower. This supports the conclusion that these variations of the surface extraction routine of MLE are effective post-processing routines for imaging of 3D ice bed tomography. Since model order statistics, measured steering vectors, and quality

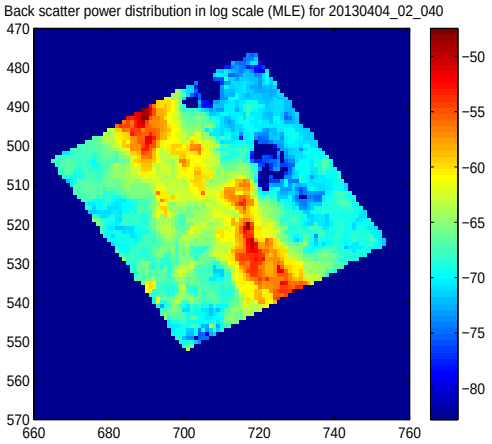

(a) Backscatter Power Distribution of Data Frame 20130404_02_040

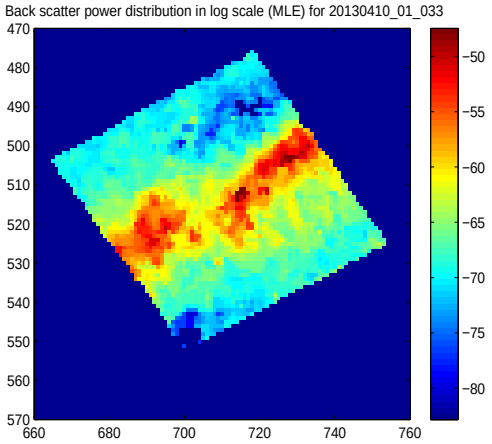

(b) Backscatter Power Distribution of Data Frame 20130410_01_033

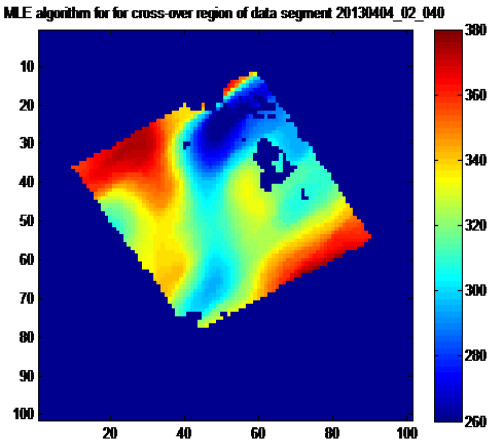

(c) Data Frame 20130404_02_040

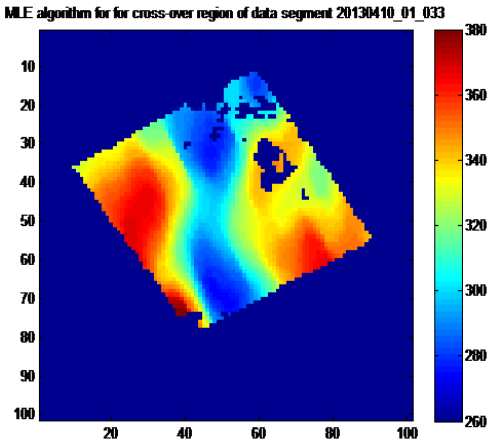

(d) Data Frame 20130410_01_033

Figure 9.14: Cross-Over Analysis by MLE With Quality Metric

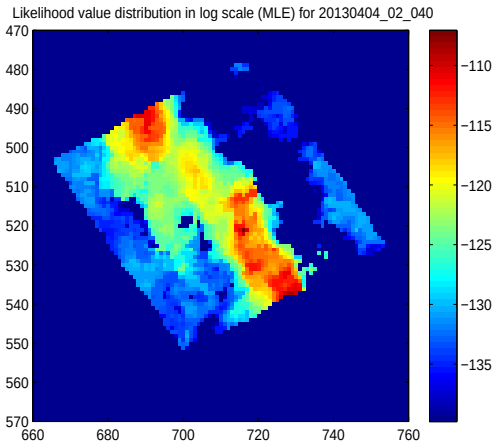

(a) Likelihood Value Distribution of Data Frame 20130404_02_040

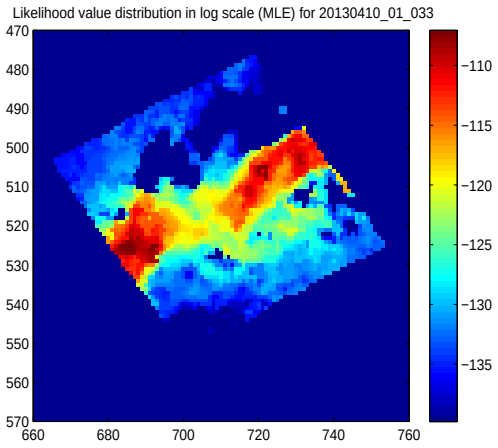

(b) Likelihood Value Distribution of Data Frame 20130410_01_033

metric incorporation do not produce significantly different results, further comparisons are needed.

Chapter 10

Conclusion and Future Work

This paper illustrates the application of DoA estimation techniques to SAR processed datasets. The fundamental approach in each of the algorithms underline a different concept with specific assumptions encompassing the system model. While the MLE algorithm resorts to a classical statistical inference model based on the likelihood function, MUSIC uses the sample correlation matrix to derive eigenspace matrices.

Although MLE has better projected performance compared to MUSIC in the low SNR regime, it is computationally the most expensive. For the antenna array geometry and sample support used in ice bed SAR tomography for this report, the surface extraction routine of MUSIC performs better than the base surface extraction routine of MLE-AP algorithm even though it does not exhibit the same probability of source separability for sources located close to each other.

We applied several techniques to improve the base surface extraction routine of the MLE approach. These are to replace ideal steering vector generation with measured steering vectors, automatic determination of the number of scatter sources, smoothing to remove outliers and reduce noise, and quality metrics to remove bad estimates. After the application of all these techniques, the surface extraction routine of MLE outperforms the surface extraction routine of MUSIC in terms of cross-over analysis. It supports the conclusion that MLE is indeed the optimal estimator for our particular ice bed tomographic application. Note that the spatial bottom smoothing aiming to

remove the artifacts made by the MLE algorithm, is the most essential step in the post-processing procedure.

For now, we are just using simple interpretation, maximization and smoothing techniques. To improve the results, we suggest the following for future work. There exists advanced surface and volume finding routines for noisy point clouds in the field of image processing and the application of these routines would very likely improve the results substantially. The surface tracking routines should incorporate the a priori knowledge that the ice bottom is generally smooth and single valued (i.e. no folding or overhangs). Currently, the surface extraction forces a single range value per direction of arrival which works well at nadir, but towards the edges of the swath it would be better to search for the best direction of arrival per range. Currently the data processing uses f-k migration for SAR processing and only a single aperture is used. Snapshots are gathered from a neighborhood of pixels. Also, we have used the narrowband approximation for the system model which is not quite valid for most of the datasets. Improved results may be obtained by the application of sub-band and sub-aperture processing to enable spatial smoothing of SAR processed datasets, coupled with enhanced clutter rejection techniques. Also, f-k migration is a Fourier based technique for applying the matched filter. While it is faster, it is not as accurate as time domain back projection which applies convolution directly because the matched filter is actually a space-time varying filter due to non-linear flight paths and sloped ice surfaces.

In conclusion, this work extends our understanding of the MLE algorithm's application to ice bottom tomography. A speed improvement to the MLE algorithm was made. We also tested the application of several post-processing routines to get the best surface out of the MLE algorithm. In this process, we developed a method for extracting measured steering vector coefficients from calibration data taken over the ocean, although the application of these coefficients did not show much change in the results. Finally, we have suggested a number of methods that might improve the results further.

References

[1] Brahima Sanou. *The world in 2013: ICT Facts and Figures*. International Telecommunications Union (ITU), February 2013.

[2] Cisco Systems. *Cisco Visual Networking Index: Global Mobile Data Traffic Forecast Update, 2012-2017*. Cisco, February 2013.

[3] Arogyaswami J. Paulraj, Dhananjay A. Gore, Rohit U. Nabar, and Helmut Bolcskei. An overview of MIMO communications - a key to gigabit wireless. *in Proceedings of the IEEE*, 92:198–218, February 2004.

[4] Thomas L. Marzetta. Noncooperative Cellular Wireless with Unlimited Numbers of Base Station Antennas. *IEEE Transactions on Wireless Communications*, 9(11):3590 – 3600, November 2010.

[5] Hoon Huh, Giuseppe Caire, Haralabos C. Papadopoulos, and Sean A. Ramprashad. Achieving "Massive MIMO" spectral efficiency with a not-so-large number of antennas. *IEEE Transactions on Wireless Communications*, 11:3226 – 3239, September 2012.

[6] Younsun Kim, Hyoungju Ji, Hyojin Lee, Juho Lee, Boon Loong Ng, and Jianzhong(Charlie) Zhang. Evolution Beyond LTE-Advanced with Full Dimension MIMO. *IEEE International Conference on Communications 2013: IEEE ICC'13 - Workshop Beyond LTE-A*, pages 111–115, June 2013.

[7] Akbar M. Sayeed and Thiagarajan Sivanadyan. Wireless Communication and Sensing in

Multipath Environments Using Multi-antenna Transceivers. *Chapter for Handbook on Array Processing and Sensor Networks, K. J. R. Liu and S. Haykin, Eds. Wiley*, 2010.

[8] M. Larsen, A. Swindlehurst, and T. Svantesson. Performance Bounds for MIMO-OFDM Channel Estimation. *IEEE Transactions on Signal Processing*, 57(5):1901–1916, May 2009.

[9] Yung-Yi Wang, Jiunn-Tsair Chen, and Wen-Hsien Fang. TST-MUSIC for joint DOA-delay estimation. *IEEE Transactions on Signal Processing*, 49(4):721–729, April 2001.

[10] A.L.F. de Almeida. *Tensor Modeling and Signal Processing for Wireless Communication Systems*. PhD. dissertation, University of Nice Sophia Antipolis (UNS), Sophia Antipolis, France, November 2007.

[11] M. Haardt and Josefa A. Nossek. Simultaneous Schur decomposition of several nonsymmetric matrices to achieve automatic pairing in multidimensional harmonic retrieval problems. *IEEE Transactions on Signal Processing*, 46(1):161–169, January 1998.

[12] Anding Wang, Lingjia Liu, and Jianzhong Zhang. Low Complexity Direction of Arrival (DoA) Esitmation for 2D Massive MIMO Systems. In *IEEE GLOBECOM Workshop on Emerging Technologies for LTE-Advanced and Beyond-4G*, December 2012.

[13] Alle-Jan van der Veen, Michaela C. Vanderveen, and Arogyaswami Paulraj. Joint angle and delay estimation using shift-invariance techniques. *IEEE Transactions on Signal Processing*, 46(2):405–418, February 1998.

[14] R. Roy and T. Kailath. ESPRIT-estimation of signal parameters via rotational invariance techniques. *IEEE Transactions on Acoustics, Speech and Signal Processing*, 37(7):984–995, July 1989.

[15] M.D. Zoltowski, M. Haardt, and C.P. Mathews. Closed-form 2-D angle estimation with rectangular arrays in element space or beamspace via Unitary ESPRIT. *IEEE Transactions on Signal Processing*, 44:316–328, February 1996.

[16] M. Haardt, F. Roemer, and G. Del Galdo. Higher-order SVD based subspace estimation to improve the parameter estimation accuracy in multi-dimensional harmonic retrieval problems. *IEEE Transactions on Signal Processing*, 56:3198–3213, July 2008.

[17] J.F. Cardoso and A. Souloumiac. Blind beamforming for non-Gaussian signals. *Radar and Signal Processing, IEE Proceedings F*, 140(6):362 – 370, December 1993.

[18] J.F. Cardoso and A. Souloumiac. Jacobi Angles For Simultaneous Diagonalization. *SIAM Journal on Matrix Analysis and Applications*, 17(1):161 – 164, January 1996.

[19] Lieven De Lathauwer, Bart De Moor, and Joos Vandewalle. Jacobi Angles For Simultaneous Diagonalization. *SIAM Journal on Matrix Analysis and Applications*, 21(4):1253 – 1278, May 1996.

[20] Yi Zhu, Lingjia Liu, Anding Wang, Krishna Sayana, and Jianzhong Zhang. DoA Estimation and Capacity Analysis for 2D Active Massive MIMO Systems. *Proceedings of the IEEE International Conference on Communications*, pages 4630 – 4634, June 2013.

[21] Jakob Hoydis, Stephan ten Brink, and Merouane Debbah. Massive MIMO: How many antennas do we need? *arXiv:1107.1709v2 [cs.IT]*, Septermber 2011.

[22] Fredrik Rusek, Daniel Persson, Buon Kiong Lau, Erik G. Larsson, Thomas L. Marzetta, Ove Edfors, and Fredrik Tufvesson. Scaling up MIMO: Opportunities and Challenges with Very Large Arrays. *arXiv:1201.3210v1 [cs.IT]*, January 2012.

[23] Ansuman Adhikary, Junyoung Nam, Jae-Young Ahn, and Giuseppe Caire. Joint Spatial Division and Multiplexing. *arXiv:1209.1402 [cs.IT]*, January 2013.

[24] A. Lee Swindlehurst and Thomas Kailath. A Performance Analysis of Subspace-Based Methods in the Presence of Model Errors: Part II - Multidimensional Algorithms. *IEEE Transactions on Signal Processing*, 41(9):2882–2890, September 1993.

[25] T.L. Marzetta. How Much Training is Required for Multiuser Mimo? *Signals, Systems and Computers, 2006. ACSSC '06. Fortieth Asilomar Conference on*, pages 359 – 363, October 2006.

[26] Song Noh, Michael D. Zoltowski, Youngchul Sung, and David J. Love. Pilot Beam Pattern Design for Channel Estimation in Massive MIMO Systems. *arXiv:1309.7430v2 [cs.IT]*, January 2014.

[27] Florian Roemer and Martin Haardt. A framework for the analytical performance assessment of matrix and tensor-based ESPRIT-type algorithms. September 2012. http://arxiv.org/abs/1209.3253.

[28] National Oceanic and Atmospheric Administration (NOAA) National Ocean Service. *Is Sea Level Rising*. June 2014.

[29] John Paden. *Synthetic aperture radar for imaging the basal conditions of the polar ice sheets*. University of Kansas, PhD Dissertation, August 2006.

[30] Sahana Raghunandan. *Analysis of Angle of Arrival Estimation Algorithms for Basal Ice Sheet Tomography*. CReSIS Techical Reports p. 57., August 2013.

[31] John Paden, Torry Akins, David Dunson, Chris Allen, and Prasad Gogineni. Ice-sheet bed 3-D tomography. *Journal of Glaciology*, 56(195):3 – 11, April 2010.

[32] J. Paden, C. Allen, and P. Gogineni. 3D imaging of ice sheets. *Geoscience and Remote Sensing Symposium (IGARSS), 2010 IEEE International*, pages 2611–2613, July 2010.

[33] R.O Schmidt. Multiple Emitter Location and Signal Parameter Estimation. *IEEE Trans. Antennas Propagation*, AP-34(3):276–280, March 1986.

[34] V. F. Pisarenko. The Retrieval of Harmonics from a Covariance Function. *Geophysical Journal of the Royal Astronomical Society*, 33(3):347 – 366, September 1973.

[35] Simon O. Haykin. *Adaptive Filter Theory, 5th Edition*. Prentice Hall, ISBN-13: 9780132671453, 2013.

[36] Harry L. Van Trees. *Optimum Array Processing (Detection, Estimation, and Modulation Theory, Part IV)*. Wiley-Interscience, 2002.

[37] I. Ziskind and M. Wax. Maximum likelihood localization of multiple sources by alternating projection. *Acoustics, Speech and Signal Processing, IEEE Transactions on*, 36(10):1553 – 1560, October 1988.

[38] P. Chen, T.-J. Wu, and J. Yang. A comparative study of model selection criteria for the number of signals. *Radar, Sonar and Navigation, IET*, 2(3):180 – 188, June 2008.

[39] Abraham. Savitzky and M. J. E. Golay. Smoothing and Differentiation of Data by Simplified Least Squares Procedures. *Analytical Chemistry*, 36(8):1627 – 1639, July 1964.